

THE ULTRALUMINOUS GRB 110918A

D. D. FREDERIKS¹, K. HURLEY², D. S. SVINKIN¹, V. D. PAL'SHIN¹, V. MANGANO^{3,4}, S. OATES⁵, R. L. APTEKAR¹, S. V. GOLENETSKII¹, E. P. MAZETS^{1,13}, PH. P. OLEYNIK¹, A. E. TSVETKOVA¹, M. V. ULANOV¹, A. V. KOKOMOV¹, T. L. CLINE^{6,14}, D. N. BURROWS³, H. A. KRIMM⁶, C. PAGANI⁷, B. SBARUFATTI^{3,8}, M. H. SIEGEL³, I. G. MITROFANOV⁹, D. GOLOVIN⁹, M. L. LITVAK⁹, A. B. SANIN⁹, W. BOYNTON¹⁰, C. FELLOWS¹⁰, K. HARSHMAN¹⁰, H. ENOS¹⁰, R. STARR⁶, A. VON KIENLIN¹¹, A. RAU¹¹, X. ZHANG¹¹, J. GOLDSTEIN¹²

Submitted to ApJ 2013-09-09, revised 2013-10-28, accepted 2013-10-29

ABSTRACT

GRB 110918A is the brightest long γ -ray burst (GRB) detected by Konus-*WIND* during its almost 19 years of continuous observations and the most luminous GRB ever observed since the beginning of the cosmological era in 1997. We report on the final Interplanetary Network localization of this event and its detailed multi-wavelength study with a number of space-based instruments. The prompt emission is characterized by a typical duration, a moderate peak energy of the time-integrated spectrum, and strong hard-to-soft evolution. The high observed energy fluence yields, at $z=0.984$, a huge isotropic-equivalent energy release $E_{\text{iso}} = (2.1 \pm 0.1) \times 10^{54}$ erg. The record-breaking energy flux observed at the peak of the short, bright, hard initial pulse results in an unprecedented isotropic-equivalent luminosity $L_{\text{iso}} = (4.7 \pm 0.2) \times 10^{54}$ erg s⁻¹. A tail of the soft γ -ray emission was detected with temporal and spectral behavior typical of that predicted by the synchrotron forward-shock model. *Swift*/XRT and *Swift*/UVOT observed the bright afterglow from 1.2 to 48 days after the burst and revealed no evidence of a jet break. The post-break scenario for the afterglow is preferred from our analysis, with a hard underlying electron spectrum and ISM-like circum-burst environment implied. We conclude that, among multiple reasons investigated, the tight collimation of the jet must have been a key ingredient to produce this unusually bright burst. The inferred jet opening angle of 1.7°–3.4° results in reasonable values of the collimation-corrected radiated energy and the peak luminosity, which, however, are still at the top of their distributions for such tightly collimated events. We estimate a detection horizon for a similar ultraluminous GRB of $z \sim 7.5$ for Konus-*WIND* and $z \sim 12$ for *Swift*/BAT, which stresses the importance of γ -ray bursts as probes of the early Universe.

Subject headings: gamma-ray burst: individual (GRB 110918A)

1. INTRODUCTION

Gamma-ray bursts (GRBs) are the brightest electromagnetic events known to occur in the Universe. The bursts last from a fraction of a second to several thousand seconds, showing a wide range of structures in their light curves and having a typical peak energy in the 100 keV–1 MeV range. The overall observed GRB fluences range from 10^{-7} to as high as 10^{-3} erg cm⁻². With the discovery of the cosmological nature of the phenomenon in 1997

(Metzger et al. 1997), it became clear that the observed flux corresponds to an enormous isotropic luminosity, making GRBs the most luminous objects in the sky. Out of the hundreds of GRBs so far observed with known redshifts, there are about a dozen with an isotropic energy release $E_{\text{iso}} \gtrsim 10^{54}$ erg; some of the most energetic events, such as GRB 080916C, seemingly released enough energy in the prompt γ -rays ($E_{\text{iso}} = 8.8 \times 10^{54}$ ergs, at $z=4.35$; Abdo et al. (2009); Greiner et al. (2009)) to constitute several times the Solar rest-mass equivalent.

The hypothesis that GRBs are non-spherical explosions implies that, when the tightly collimated relativistic fireball is decelerated by the circum-burst medium down to the Lorentz factor $\Gamma \sim 1/\theta_{\text{jet}}$ (where θ_{jet} is the jet opening angle), an achromatic break (jet break) should appear, in the form of a sudden steepening in the GRB afterglow light curve, at a characteristic time t_{jet} . The steepening is caused by the combination of the jet edge effect, and the possible relativistic sideways expansion effect (Rhoads 1999; Sari et al. 1999; Panaitescu & Mészáros 1999; Zhang & Mészáros 2004). In the canonical light curve of X-ray afterglows (Zhang et al. 2006; Nousek et al. 2006) the jet break corresponds to a transition from the “normal” segment III to the post-break, “jet” segment IV. With typical collimation angles of a few degrees, the true energy release from most GRBs is $\sim 10^{51}$ ergs, on par with that of a supernova (Frail et al. 2001).

The long-duration, extremely intense GRB 110918A

¹ Ioffe Physical-Technical Institute, Politekhnikeskaya 26, St. Petersburg 194021, Russia; fred@mail.ioffe.ru

² Space Sciences Laboratory, University of California, 7 Gauss Way, Berkeley, CA 94720-7450, USA

³ Pennsylvania State University, Department of Astronomy and Astrophysics, College Park, PA 16801, USA

⁴ INAF-IASFPA, Via Ugo La Malfa 153, 90146 Palermo, Italy

⁵ Mullard Space Science Laboratory, University College London, Holmbury St. Mary, Dorking, Surrey RH5 6NT, UK

⁶ NASA Goddard Space Flight Center, Greenbelt, MD 20771, USA

⁷ U. Leicester, University Road, Leicester, LE1 7RH, UK

⁸ INAF-OAB, via Bianchi 46, 23807, Merate (LC), Italy

⁹ Space Research Institute, Profsoyuznaya 84/32, Moscow 117997, Russia

¹⁰ Department of Planetary Sciences, University of Arizona, Tucson, AZ 85721, USA

¹¹ Max-Planck-Institut für extraterrestrische Physik, Giessenbachstrasse, Postfach 1312, D-85748 Garching, Germany

¹² Applied Physics Laboratory, Johns Hopkins University, Laurel, MD 20723, USA

¹³ Deceased

¹⁴ Emeritus

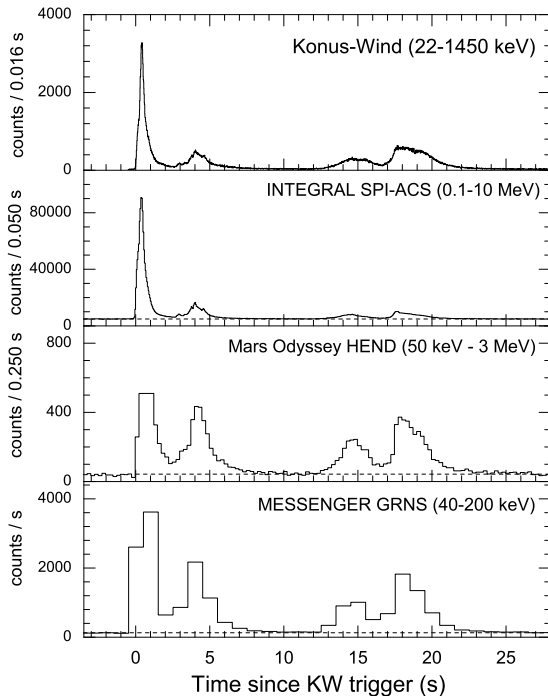


Figure 1. GRB 110918A light curves recorded by the four IPN instruments. The time scale is corrected for the burst propagation between the spacecraft. The Konus-*WIND* trigger time corresponds to the Earth-crossing time 77218.928 s UT (21:26:58.928)

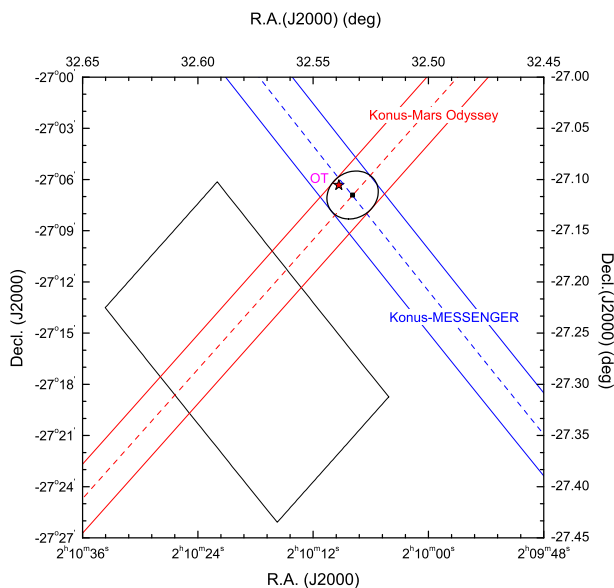


Figure 2. Initial IPN error box of GRB 110918A, the refined annuli, the error ellipse, and the X-ray/optical counterpart (indicated by the star).

was detected by *INTEGRAL* (SPI-ACS), *Konus-WIND*, *Mars Odyssey* (HEND), and *MESSENGER* (GRNS). At the time of the burst, *Swift* was in the South Atlantic Anomaly and Earth-occulted; *Fermi* was also Earth-

occulted. Using the Interplanetary Network (IPN), a location was determined (Hurley et al. 2011). A preliminary analysis of the *Konus-WIND* detection revealed that GRB 110918A is the most intense γ -ray burst observed by the instrument since it began operation in 1994 November (Golenetskii et al. 2011).

Swift/XRT began follow-up observations ~ 1.2 days after the trigger and was able to observe and localize an X-ray counterpart to this burst (Mangano et al. 2011a). The XRT source was found outside the 3σ initial IPN error box at $640''$ from its center. The optical afterglow (Tanvir et al. 2011) was monitored by *Swift*/UVOT (Siegel et al. 2011) and by a multitude of ground-based telescopes (Elliott et al. 2011; Cenko et al. 2011; Levan et al. 2011; Oksanen et al. 2011; Guidorzi et al. 2011; Perley et al. 2011a; Elliott et al. 2013). No sub-mm flux was detected from the source, with a 3-sigma upper limit of 15 mJy, in the APEX/LABOCA observations performed at 345 GHz (de Ugarte Postigo et al. 2011a). The best optical counterpart position is from GROND (Elliott et al. 2013) at a location R.A. (J2000) = $02^h 10^m 09.34^s$, Decl. (J2000) = $-27^\circ 06' 19.7''$ with an error of $0.2''$. Using the GMOS-N spectrograph on Gemini-N, Mauna Kea, Levan et al. (2011) determined a spectroscopic redshift of $z = 0.982$. This was later confirmed by de Ugarte Postigo et al. (2011b) with the GTC telescope at Roque de los Muchachos Observatory, who reported $z = 0.984 \pm 0.001$.

At this redshift, the huge energy flux measured by *Konus-WIND* implied equally enormous values of the isotropic-equivalent energy released in the source frame, $E_{\text{iso}} \sim 1.9 \times 10^{54}$ erg, and an isotropic-equivalent peak luminosity $L_{\text{iso}} \sim 4.4 \times 10^{54} \text{ erg s}^{-1}$ (Frederiks & Pal'shin 2011). These preliminary estimates place GRB 110918A among the several brightest events ever observed in the era of cosmological GRBs and, accordingly, this burst merits a more detailed consideration.

The main goal of this article is to give a comprehensive coverage of GRB 110918A observations made with space-based instruments. In Section 2.1, we start with an analysis of the IPN localization, discuss the spacecraft timing issues and provide corrected annuli, which form a refined error ellipse. In Sections 2.2 and 2.3, we give a detailed description and analysis of the prompt and extended γ -ray emission detected by *Konus-WIND*. In Section 2.4, we report on results of X-ray afterglow observations made with *Swift*-XRT and UV/optical observations with *Swift*-UVOT. Finally, we discuss these results in the context of the burst cosmological rest frame and put constraints on the collimation angle and the collimation-corrected energy of GRB 110918A. In a companion paper, (Elliott et al. 2013), hereafter E13, discuss the ground-based optical observations of this event and its host galaxy.

Throughout the paper all errors reported are 90% conf. levels unless otherwise specified. The power-law temporal decay slopes, α , and power-law spectral indices, β , are defined such that the flux density $F_\nu(t) \propto t^{-\alpha}$ and $F_\nu \propto \nu^{-\beta}$, respectively; also, to avoid a confusion with the Band spectral model parameters, the use of α and β is explicitly stated where appropriate. We adopt the conventional notation $Q_k = Q/10^k$, and use cgs units unless otherwise noted.

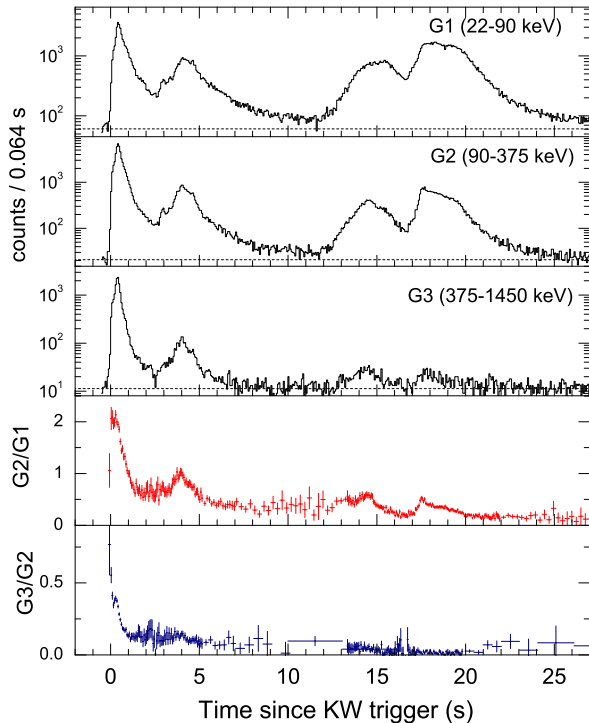


Figure 3. Light curves of GRB 110918A recorded by Konus-WIND in the G1, G2 and G3 energy bands with 64 ms resolution (three upper panels). The count rates are dead-time corrected; background levels are indicated by dashed lines. An apparent hardness-intensity correlation and a general emission softening in the course of the burst are illustrated by the evolution of the hardness ratios ($G2/G1$ and $G3/G2$) shown in the two lower panels.

2. OBSERVATIONS AND ANALYSES

2.1. IPN Observations and Localization

GRB 110918A was detected by four IPN: *INTEGRAL* SPI-ACS (Rau et al. 2005), in a highly elliptical orbit, Konus-WIND (Aptekar et al. 1995), in orbit around the Lagrangian point L1, *MESSENGER* GRNS (Gold et al. 2001), in orbit around Mercury, and *Mars Odyssey* HEND (Hurley et al. 2006), in orbit around Mars, at 0.46, 5.0, 645.9, and 943.0 light-seconds from Earth, respectively. The light curve of the event (Figure 1) starts with an extremely bright, hard, and short pulse followed by three weaker, softer, and partly overlapping pulses in the next 25 seconds.

An initial 62 sq. arcmin IPN error box was derived using Konus-WIND, *MESSENGER*, and *Odyssey*, and was announced in a GCN Circular (Hurley et al. 2011). A *Swift* target-of-opportunity observation was requested; when the XRT position was announced (Mangano et al. 2011a) it was evident that the error box was significantly displaced from the counterpart. After lengthy investigation, it was found that both the *MESSENGER* and *Odyssey* times were inaccurate due to the use of outdated spacecraft clock files. With the updated files, and with *INTEGRAL* added, the burst was triangulated again, and an error ellipse was derived using the

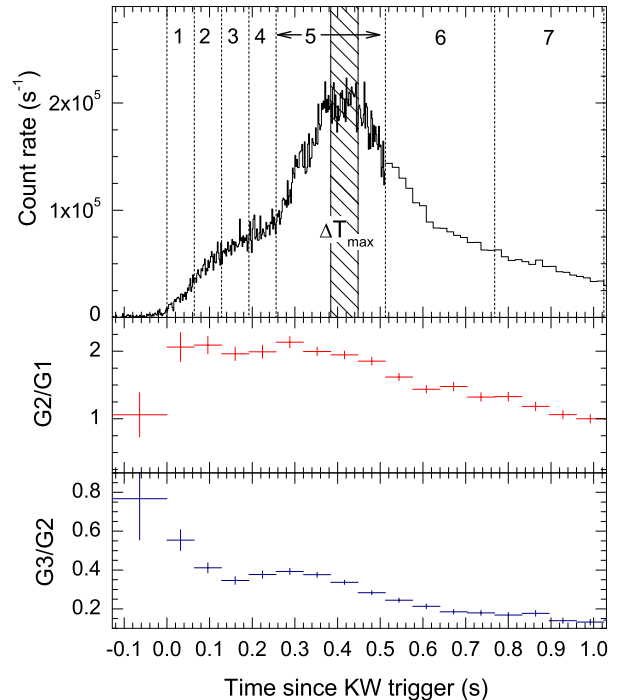


Figure 4. Initial pulse, P_1 . Konus-WIND light curve in the G1+G2+G3 (22–1450 keV) band is shown with a 2 ms (16 ms after $T_0 + 0.512$ s) resolution. Accumulation intervals for the KW time-resolved spectra 1–7 are indicated with the vertical dashed lines. The 64 ms interval ΔT_{\max} has been used for the peak energy flux calculation. The hardness ratios are shown in the two lower panels.

method described in Hurley et al. (2000). The 3σ ellipse has major axis 3.16 arcmin, minor axis 1.2 arcmin, and area 2.6 sq. arcmin; the ellipse is centered at R.A.(J2000)= $02^h 10^m 07.9s$, Decl.(J2000)= $-27^\circ 06' 54.4''$, with $\chi^2 = 0.06$ for 1 degree of freedom (d.o.f.; three annuli minus two fitted coordinates). The optical counterpart found by Tanvir et al. (2011) lies inside the ellipse, 0.66 arcmin from its center (Figure 2).

2.2. Konus-WIND Observation and Analysis

GRB 110918A triggered the Konus-WIND γ -ray spectrometer (KW) at $T_0(KW)=77222.856$ s UT (21:27:02.856) on 2011 September 18, hereafter T_0 . It was detected by the S1 detector, which observes the Southern ecliptic hemisphere; the incident angle was $53^\circ 1'$. The propagation delay from Earth to WIND is 3.928 s for this GRB, correcting for this factor, the KW trigger time corresponds to the Earth-crossing time 77218.928 s UT (21:26:58.928).

2.2.1. Time History

In the instrument’s “triggered mode”, count rates are recorded in three energy bands: G1(22–90 keV), G2(90–375 keV), and G3(375–1450 keV). The record starts at $T_0 - 0.512$ s and continues to $T_0 + 229.376$ s with an accumulation time varying from 2 to 256 ms. The “background mode” count rate data are available up to $T_0 + 250$ s in the same energy bands with a coarse resolution of 2.944 s.

The prompt-emission light curve (Figure 3) can be divided into two groups of overlapping pulses, which are separated by a minimum around $\sim T_0 + 11.5$ s when the observed rate in the harder G2 and G3 bands is comparable to the background level. The first group, hereafter referred as Phase I, is characterized by two pronounced pulses: the huge P_1 , which peaks at $\sim T_0 + 0.368$ s, and P_2 ($\sim T_0 + 4.032$ s); the second group (Phase II) is comprised of considerably overlapping pulses P_3 ($\sim T_0 + 14.6$ s) and P_4 ($\sim T_0 + 17.7$ s). Shown in the same figure, the temporal evolution of the G2/G1 and G3/G2 hardness ratios indicates an apparent hardness-intensity correlation of the emission against a general tendency of spectral softening in the course of the burst.

The bright, pulsed emission decays up to $\sim T_0 + 30$ s. However, a stable excess in the count rate over the background level was detected, mostly in the softer G1 and G2 energy bands, until $T_0 + 250$ s when the KW measurements stopped due to the limited capacity of the *WIND* spacecraft telemetry. The detailed analysis of the extended γ -ray emission is given in Section 2.3.

The burst starts with a sharp rise of the bright, hard, short pulse P_1 which culminates after a ~ 350 ms two-step onset (Figure 4). In this phase, a spectrum with high and evolving peak energy is suggested by the hardness ratio behavior: the G3/G2 ratio rapidly decays from a maximum at the onset of the initial pulse, while G2/G1 remains at a high, but stable level until $\sim T_0 + 0.370$ s, when a peak of the emission is reached. The observed count rate of $\sim 2 \times 10^5$ s $^{-1}$ in the cumulative G1+G2+G3 (22–1450 keV) energy band is unprecedented in almost 19 years of KW observations of long γ -ray bursts. Although the photon flux is very high, a standard KW dead-time correction procedure (i.e., a simple non-paralyzable dead-time correction in each of the measurement bands, taking into account a softer gate blocking by harder ones) is still applicable to the burst; no additional modeling, which was used, e.g., in an analysis of the KW detection of the 1998 August 27 giant flare from SGR 1900+14, is required (details of these simulations and the KW dead-time correction procedures can be found in Mazets et al. 1999).

The trailing edge of the initial pulse is more gently sloping; the emission intensity decreases until $T_0 + 2.5$ s and gives way, with a small “bump” at $\sim T_0 + 2.95$ s, to the rise of the second, relatively weaker, and softer pulse, P_2 . The G1+G2+G3 count rate in this pulse reaches a 64 ms peak value of $\sim 3 \times 10^4$ s $^{-1}$ (or ~ 0.15 of that in P_1) at $T_0 + 4.032$ s and then gradually decays to a minimum around $\sim T_0 + 11.5$ s, which separates Phase I and Phase II.

A new rise begins at $\sim T_0 + 11.5$ s. The third (P_3) and fourth (P_4) pulses form an overlapping structure (Phase II) in the time interval from $T_0 + 11.5$ s to $\sim T_0 + 25$ s. The peak 64-ms count rate reached in these two pulses is $\sim 1.9 \times 10^4$ s $^{-1}$ and $\sim 3.8 \times 10^4$ s $^{-1}$, respectively. While these rates are on par with that in the second pulse, P_2 , the hardness ratios indicate a considerably softer emission spectrum. Despite the huge count rate in the initial pulse, the count fluence recorded by KW in the 22–1450 keV band during the first ~ 25 seconds of the burst is nearly equally divided between Phase I and Phase II.

In the G2+G3 energy band (90–1450 keV), standard

Table 1
Spectral Lags between Konus-*WIND* Light Curves

Time Interval from T_0 (s)	Light Curves	τ_{lag}^a (s)
-0.032–26.368	G3–G1	0.092 ± 0.003^b
	G2–G1	0.047 ± 0.002
	G3–G2	0.047 ± 0.002
-0.032–2.000 (Initial pulse)	G3–G1	0.091 ± 0.003
	G2–G1	0.043 ± 0.002
	G3–G2	0.047 ± 0.002
-0.032–8.000 (Phase I)	G3–G1	0.092 ± 0.003
	G2–G1	0.044 ± 0.002
	G3–G2	0.047 ± 0.002
12.096–26.368 (Phase II)	G3–G1	0.36 ± 0.13
	G2–G1	0.19 ± 0.01
	G3–G2	0.09 ± 0.05

^a Positive spectral lag τ_{lag} means that the spectrum has hard to soft evolution.

^b 1σ uncertainties throughout this table.

for calculations of the KW GRB light curve characteristics, the total duration of the burst, determined at the 5σ level, is $T_{100} = 95.154$ s (from $T_0 - 0.178$ s to $T_0 + 94.976$ s). The corresponding T_{90} value is 19.6 ± 0.1 s and $T_{50} = 14.3 \pm 0.1$ s. The G2+G3 count rate reached a maximum of $(1.46 \pm 0.02) \times 10^5$ s $^{-1}$ in the 64 ms bin starting 0.368 s after the trigger, and the total number of counts during the T_{100} interval is 1.34×10^5 .

2.2.2. Spectral Lags

The observed evolution of the hardness ratios suggests that soft photons are delayed with respect to the higher energy ones, a common property of long GRBs. We examined the spectral lag τ_{lag} using the cross-correlation function (CCF) between the light curves in two energy bands (Norris et al. 2000; Band 1997). After calculating the CCF as a function of τ_{lag} we obtained the peak value of τ_{lag} by fitting it with a fourth-degree polynomial.

The resulting values of τ_{lag} between the 16 ms G1, G2, and G3 light curves at different phases of the burst are listed in Table 1. Statistically significant lags in the 40 – 360 ms range are derived for the initial pulse (P_1), Phase I, Phase II, and in the entire prompt phase of the emission. The positive τ_{lag} ’s are indicative of hard-to-soft spectral evolution.

Predictably, the lags for the entire burst and Phase I are almost identical to the lags found for the huge initial pulse alone. However, for the soft Phase II, the values of τ_{lag} are two-to-four times longer than for the hard initial phase of the event.

2.2.3. Light-curve Decomposition

The prompt emission of long GRBs shows a wide range of structures in its light curve. Attempts have been made to fit the light curves with Fast Rise Exponential Decay models described by combinations of power-law functions (Kocevski & Liang 2003; Kocevski et al. 2003), exponential functions (Norris et al. 1996; Lee et al. 2000a,b; Norris et al. 2005), and log-normal functions (Bhat et al. 2012).

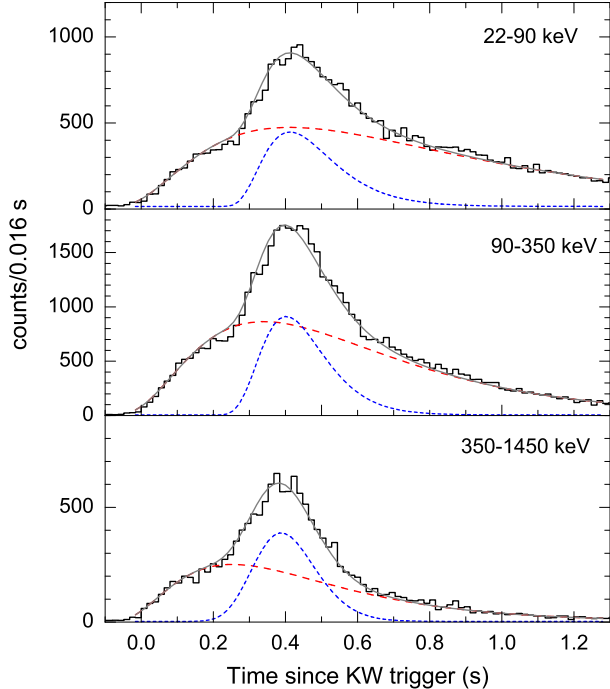


Figure 5. Decomposition of the initial pulse light curve. The background-subtracted 16 ms light curves in the G1, G2, and G3 bands are best fit by two components, each described by the four-parameter exponential model. The components C_1 and C_2 are shown with long and short dashes, respectively; the sum of the components is shown with a solid line.

The light curve of the initial pulse (Figure 4) shows a clear two-step onset, which suggests at least two overlapping episodes of emission. We performed the analysis of this pulse with the background-subtracted G1, G2, and G3 light curves using the four-parameter exponential model from Norris et al. (2005):

$$A(t) = A_m \lambda \exp\{-\tau_1/(t - t_0) - (t - t_0)/\tau_2\} \quad (1)$$

for $t > t_0$, where $\lambda = \exp(2\mu)$, $\mu = (\tau_1/\tau_2)^{1/2}$. A_m is the pulse amplitude, t_0 is the pulse start time, and τ_1 , τ_2 are time constants characterizing the rise and decay parts of the pulse. This pulse peaks at $t_m = t_0 + (\tau_1\tau_2)^{1/2}$ and has a width measured between two $1/e$ points, $w = \tau_2(1 + 4\mu)^{1/2}$.

The 16 ms light curves have been fitted in the $T_0 - T_0 + 1.3$ s interval with a single pulse, two, and more overlapping components using a χ^2 statistic. The single-component model yields very high χ_r^2 . Introducing the second component improved the fit dramatically: χ^2 changed from 1123/78 d.o.f. to 132/74 d.o.f. for the G2 light curve. A similar improvement is found for the G1 and G3 light curves. Further addition of components to the model results in ambiguous, poorly constrained fits and does not improve the statistic. Thus, we conclude that the KW light curves of the initial pulse are best described by the double-component model.

Figure 5 shows the decomposition and Table 2 lists the model parameters and the derived quantities. The

narrow component C_2 , which dominates at the peak of the emission in the harder bands, is delayed with respect to a wider component C_1 , which describes the onset of the initial pulse before $\sim T_0 + 0.2$ s and its decay after $\sim T_0 + 0.8$ s. The delays between the components, calculated as the difference between their peak times, t_m , are ~ 0 ms, ~ 62 ms, and ~ 136 ms in the G1, G2, and G3 bands, respectively. In the same way, we calculated lags between the G1, G2, and G3 bands for each component. The G3-G1, G2-G1, and G3-G2 lags for the leading sub-pulse C_1 (160 ± 10 ms, 72 ± 8 ms, and 87 ± 8 ms, respectively) are ~ 7 times longer than the corresponding lags for C_2 (24 ± 7 ms, 10 ± 5 ms, and 14 ± 6 ms, respectively). The relatively longer lags obtained for the leading component are in agreement with the strong evolution of the G3/G2 hardness ratio present in the first ~ 300 ms of the burst.

Since a rapid variability in GRB light curves could be linked directly to the activity of the central engine (Sari & Piran 1997; Kobayashi et al. 1997; Ryde 2004), the shortest variability timescale for a gamma-ray burst is clearly of interest. In particular, assuming that the shortest timescale in GRB prompt emission is the shortest pulse width, the length scale of the GRB central engine can be estimated (see, e.g., Bhat et al. (2012) and references therein). For GRB 110918A, we find a width of $\delta T \equiv w = 0.25$ s, obtained for the sub-pulse C_2 in the energy bands G2 and G3.

2.2.4. Time-resolved Spectral Analysis

In the triggered mode, *Konus-WIND* measures 64 energy spectra in 128 channels of two overlapping energy bands: PHA1 (22–1450 keV) and PHA2 (375 keV–18 MeV). The first four spectra have a fixed accumulation time of 64 ms; after that, the accumulation time varies over 0.256–8.192 s, depending on the current intensity of the burst. During the bright prompt phase of GRB 110918A, 35 energy spectra were measured: 17 of them covered the first hard pair of pulses ($T_0 - T_0 + 5.632$ s), and spectrum 18 was recorded during the temporary decrease in the burst intensity ($T_0 + 5.632 - T_0 + 13.312$ s); the remaining 17 spectra ($T_0 + 13.312 - T_0 + 28.416$ s) covered the second soft group of pulses and the transition to the extended emission tail.

The spectral analysis was performed with XSPEC, version 12.5 (Arnaud 1996) with the Band GRB function (Band et al. 1993): $f(E) \propto E^\alpha \exp(-(2 + \alpha)E/E_{\text{peak}})$ for $E < E_{\text{peak}}(\alpha - \beta)/(2 + \alpha)$, and $f(E) \propto E^\beta$ for $E \geq E_{\text{peak}}(\alpha - \beta)/(2 + \alpha)$ where α is the power-law photon index, E_{peak} is the peak energy in the νF_ν spectrum, and β is the photon index at higher energies. The spectral model was normalized to the energy flux in the 20 keV–10 MeV range, a standard band for the KW GRB spectral analysis.

Typically, the raw count rate spectra were rebinned to have at least 20 counts per energy bin to ensure Gaussian-distributed errors and the correctness of the χ^2 statistic. Spectra 3, 4, and 5 have good count statistics in the MeV band, which allowed us to study the hard emission with a minimal channel binning. For these spectra, the `cstat` and `pgstat` options of XSPEC were also used and we found the fit results to be consistent with those obtained by the first method. At the very high count rate observed in the GRB 110918A initial pulse,

Table 2
Initial Pulse Decomposition

Light curve	A_m (10^3 counts s^{-1})	t_0 (s)	τ_1 (s)	τ_2 (s)	t_m (s)	w (s)
Component C_1						
G1	28.7 ± 0.3	-0.144 ± 0.002	0.631 ± 0.009	0.491 ± 0.005	0.412 ± 0.007	1.154 ± 0.012
G2	53.7 ± 0.4	-0.157 ± 0.001	0.801 ± 0.007	0.307 ± 0.002	0.339 ± 0.005	0.839 ± 0.005
G3	15.5 ± 0.2	-0.150 ± 0.003	0.648 ± 0.011	0.250 ± 0.003	0.262 ± 0.007	0.682 ± 0.007
Component C_2						
G1	27.1 ± 0.7	0.177 ± 0.003	0.706 ± 0.021	0.079 ± 0.002	0.413 ± 0.004	0.283 ± 0.006
G2	56.7 ± 1.1	0.137 ± 0.002	1.221 ± 0.020	0.057 ± 0.001	0.402 ± 0.003	0.253 ± 0.003
G3	24.1 ± 0.6	-0.179 ± 0.002	12.418 ± 0.107	0.026 ± 0.001	0.388 ± 0.005	0.244 ± 0.002

Table 3
Konus-WIND Time-resolved Spectral Fits with the Band Function

Spectrum	Accumulation Interval (s from T_0)	α	β	E_{peak} (keV)	Flux ^a (10^{-6} erg cm^{-2} s^{-1})	$\chi^2/\text{d.o.f.}$
1	0–0.064	$-0.75^{+0.10}_{-0.09}$	-2.35^b	4050^{+1610}_{-2770}	290^{+20}_{-19}	22.7/25
2	0.064–0.128	$-0.67^{+0.10}_{-0.09}$	-2.35^b	1630^{+330}_{-270}	348^{+21}_{-20}	33.3/33
3	0.128–0.192	$-0.68^{+0.11}_{-0.18}$	$-2.49^{+0.29}_{-0.40}$	1230^{+300}_{-260}	370^{+32}_{-30}	65.3/75 ^c
4	0.192–0.256	$-0.54^{+0.13}_{-0.09}$	$-2.23^{+0.23}_{-0.26}$	1160^{+330}_{-300}	487^{+40}_{-37}	76.7/77 ^c
5	0.256–0.512	$-0.47^{+0.09}_{-0.08}$	$-2.39^{+0.11}_{-0.14}$	1120^{+160}_{-150}	775^{+27}_{-26}	92.4/86 ^c
6	0.512–0.768	$-0.44^{+0.11}_{-0.10}$	$-2.45^{+0.09}_{-0.10}$	443^{+45}_{-41}	289^{+12}_{-12}	77.2/57
7	0.768–1.024	$-0.48^{+0.17}_{-0.15}$	$-2.48^{+0.15}_{-0.16}$	290^{+40}_{-32}	$125^{+6.8}_{-6.8}$	30.3/50
8	1.024–1.280	$-0.88^{+0.18}_{-0.14}$	$-2.39^{+0.23}_{-0.27}$	270^{+62}_{-45}	$51.5^{+4.5}_{-4.4}$	31.2/44
9	1.280–1.536	$-1.26^{+0.14}_{-0.14}$	$-2.37^{+0.22}_{-2.60}$	294^{+118}_{-62}	$24.6^{+3.7}_{-4.4}$	54.2/74
10	1.536–2.304	$-1.34^{+0.15}_{-0.11}$	$-2.33^{+0.16}_{-0.56}$	260^{+74}_{-51}	$13.1^{+2.0}_{-1.7}$	52.7/50
11	2.304–3.328	$-1.25^{+0.10}_{-0.09}$	$-2.58^{+0.24}_{-0.53}$	261^{+43}_{-35}	$10.9^{+1.2}_{-1.1}$	51.1/51
12	3.328–3.840	$-0.98^{+0.12}_{-0.11}$	$-2.89^{+0.32}_{-1.85}$	301^{+51}_{-40}	$24.8^{+2.1}_{-2.2}$	65.5/48
13	3.840–4.096	$-0.97^{+0.11}_{-0.10}$	$-2.75^{+0.28}_{-0.87}$	378^{+58}_{-53}	$48.7^{+4.3}_{-4.7}$	68.5/44
14	4.096–4.352	$-1.00^{+0.14}_{-0.11}$	$-2.78^{+0.21}_{-0.61}$	300^{+45}_{-48}	$41.1^{+3.4}_{-3.4}$	46.6/43
15	4.352–4.608	$-0.86^{+0.30}_{-0.18}$	$-2.49^{+0.19}_{-0.29}$	205^{+45}_{-44}	$33.7^{+3.3}_{-3.0}$	36.6/41
16	4.608–4.864	$-0.69^{+0.28}_{-0.24}$	$-2.29^{+0.11}_{-0.15}$	155^{+31}_{-23}	$29.2^{+3.0}_{-2.8}$	40.7/39
17	4.864–5.632	$-1.28^{+0.16}_{-0.13}$	$-2.44^{+0.16}_{-0.28}$	150^{+26}_{-22}	$12.1^{+1.2}_{-1.2}$	38.9/47
18	5.632–13.312	$-1.33^{+0.18}_{-0.14}$	$-2.60^{+0.17}_{-0.27}$	90^{+9}_{-9}	$1.94^{+0.18}_{-0.16}$	63.8/82
19	13.312–14.080	$-0.79^{+0.25}_{-0.20}$	$-2.68^{+0.15}_{-0.20}$	99^{+9}_{-9}	$9.69^{+0.73}_{-0.66}$	29.5/44
20	14.080–14.336	$-0.60^{+0.36}_{-0.28}$	$-2.68^{+0.20}_{-0.31}$	116^{+16}_{-15}	$16.2^{+1.7}_{-1.5}$	28.0/34
21	14.336–14.592	$-0.64^{+0.26}_{-0.21}$	$-2.99^{+0.26}_{-0.43}$	119^{+11}_{-11}	$17.5^{+1.5}_{-1.3}$	28.8/33
22	14.592–14.848	$-0.87^{+0.24}_{-0.22}$	$-3.28^{+0.38}_{-2.30}$	111^{+12}_{-10}	$15.8^{+1.3}_{-1.2}$	29.1/33
23	14.848–15.360	$-0.96^{+0.18}_{-0.15}$	$-3.58^{+0.39}_{-0.83}$	85^{+5}_{-5}	$12.9^{+0.63}_{-0.58}$	26.0/38
24	15.360–16.128	$-1.12^{+0.26}_{-0.21}$	$-3.11^{+0.19}_{-0.29}$	59^{+3}_{-3}	$9.99^{+0.45}_{-0.42}$	37.0/39
25	16.128–17.664	$-1.39^{+0.10}_{-0.10}$	< -3.39	68^{+3}_{-4}	$9.63^{+0.32}_{-0.33}$	37.8/51
26	17.664–17.920	$-0.73^{+0.28}_{-0.22}$	$-3.68^{+0.46}_{-1.35}$	95^{+6}_{-6}	$26.3^{+1.5}_{-1.4}$	37.7/33
27	17.920–18.176	$-0.64^{+0.25}_{-0.18}$	< -3.70	87^{+4}_{-5}	$23.2^{+1.0}_{-0.95}$	33.9/31
28	18.176–18.432	$-0.73^{+0.28}_{-0.24}$	$-3.78^{+0.43}_{-0.83}$	81^{+5}_{-5}	$23.9^{+1.0}_{-1.00}$	42.6/30
29	18.432–18.688	$-0.66^{+0.22}_{-0.22}$	$-3.65^{+0.34}_{-0.73}$	82^{+5}_{-4}	$22.9^{+1.0}_{-1.0}$	32.9/29
30	18.688–18.944	$-0.81^{+0.23}_{-0.22}$	< -3.75	81^{+5}_{-5}	$20.9^{+0.92}_{-0.91}$	16.6/27
31	18.944–19.200	$-0.67^{+0.21}_{-0.21}$	< -4.01	75^{+4}_{-3}	$19.4^{+0.78}_{-0.82}$	33.9/29
32	19.200–19.456	$-0.62^{+0.32}_{-0.29}$	$-3.82^{+0.40}_{-2.04}$	71^{+4}_{-4}	$19.1^{+0.84}_{-0.82}$	21.3/29
33	19.456–19.712	$-0.75^{+0.34}_{-0.28}$	$-3.67^{+0.38}_{-0.73}$	67^{+4}_{-4}	$18.1^{+0.92}_{-0.87}$	22.7/27
34	19.712–20.224	$-0.98^{+0.33}_{-0.22}$	$-3.63^{+0.34}_{-0.59}$	52^{+3}_{-3}	$13.0^{+0.57}_{-0.47}$	34.6/35
35	20.224–28.416	$-1.50^{+0.38}_{-0.31}$	$-3.11^{+0.18}_{-0.25}$	34^{+8}_{-10}	$1.46^{+0.075}_{-0.076}$	80.1/94

^a In the 20 keV–10 MeV energy band.

^b Spectra 1 and 2 were fitted with index β fixed to that of the time-averaged spectrum 1+2, for which: $\alpha = -0.68^{+0.10}_{-0.08}$, $\beta = -2.35^{+0.32}_{-0.79}$, and $E_{\text{peak}} = 2290^{+610}_{-540}$ ($\chi^2 = 61.6/57$ d.o.f.)

^c PG-statistic/d.o.f.

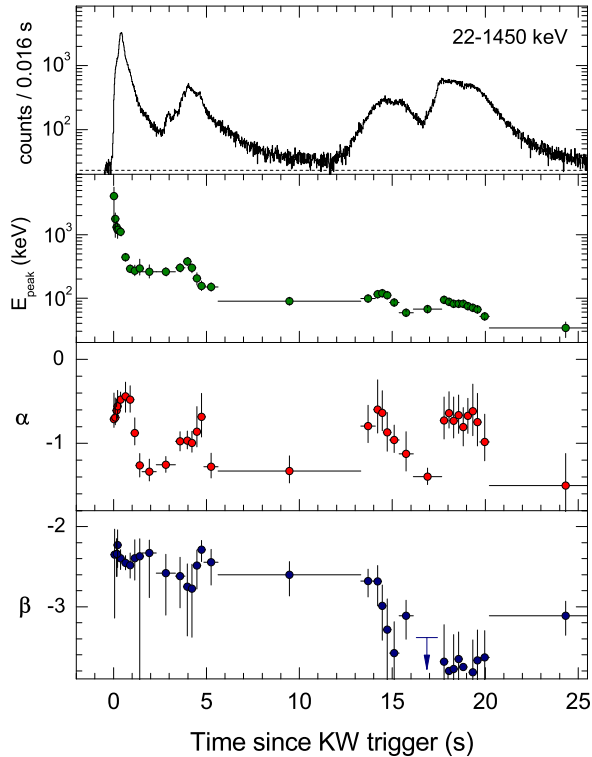


Figure 6. Spectral evolution of the γ -ray emission during the prompt phase of the burst. The Konus-*WIND* light curve in the combined G1+G2+G3 energy band (22–1450 keV) is shown with 16 ms resolution, along with the temporal behavior of the Band spectral model parameters E_{peak} , α and β obtained from the time-resolved fits (see Table 3).

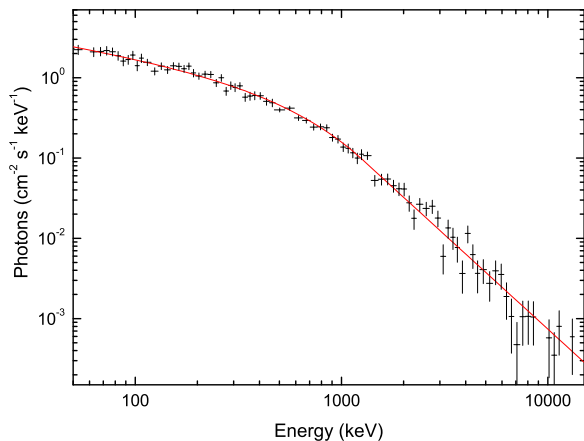


Figure 7. Photon spectrum at the culmination of the initial pulse ($T_0+0.256 - T_0+0.512$; the model parameters are given in Table 3). The emission is traced to > 10 MeV with no obvious high-energy cutoff observed up to the KW upper energy threshold.

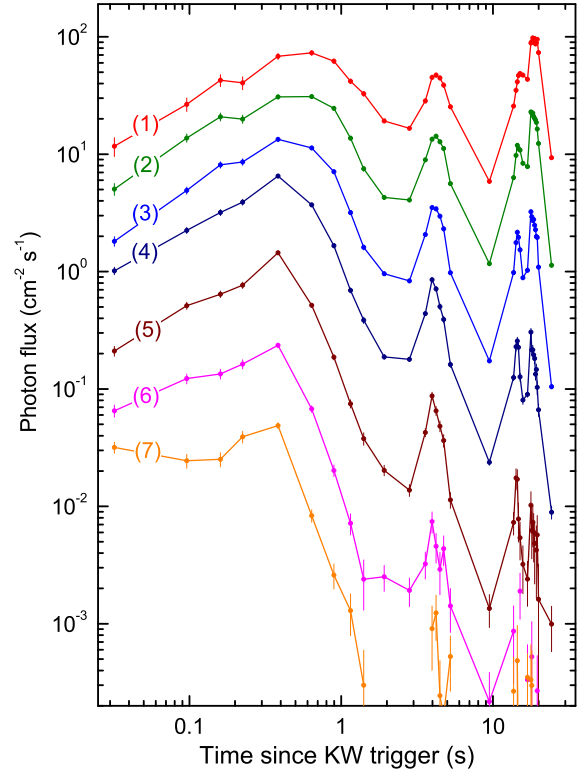


Figure 8. Evolution of the photon flux during the prompt phase of GRB 110918A. The flux is calculated from the KW time-resolved spectral fits and plotted vs. time for the following energy ranges: 20–50 keV (plot 1), 50–100 keV (2), 100–200 keV (3), 200–500 keV (4), 500–1000 keV (5), 1–2 MeV (6), and 2–18 MeV (7). The plots, except (1), are consecutively scaled down by half an order of magnitude for viewing convenience.

the differential nonlinearity (DNL) of the instrument’s analog-to-digital converters must be taken into account as a source of systematic errors in the count spectra. To account for the known level of uncertainty in the DNL, we added up to 25% systematics to statistical errors for 256-ms spectra covering the initial pulse. Also, channels below 50 keV were excluded from fits for spectrum 5 since the influence of a pulse-pileup effect on the low-energy part of this spectrum is not negligible. The same precautions were taken for time-averaged spectra, which include the initial pulse.

Results of the KW time-resolved spectral analysis are listed in Table 3. A good quality of fit is achieved for the majority of the spectra, which enables us to construct the temporal behavior of the model parameters (α , β , E_{peak}) and to trace in detail the evolution of the spectral composition of radiation over the course of the burst (Figure 6).

Spectra 1–4 were measured at the onset of the extremely intense initial pulse (Figure 4). The emission at this moment is very hard; E_{peak} reaches the highest value for the burst (~ 4 MeV) in the first 64-ms interval after the trigger. As the intensity surges up, E_{peak} starts to decrease gradually, but the flattening

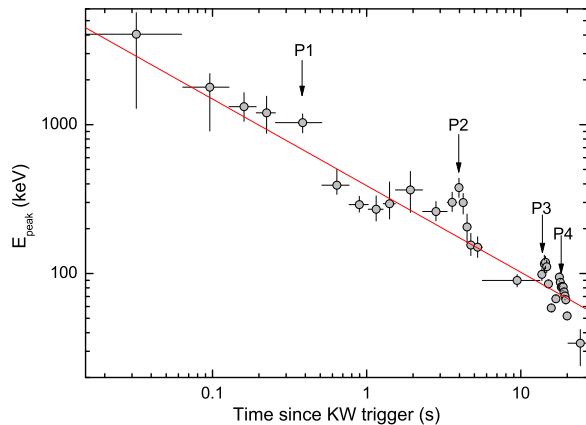


Figure 9. General trend of E_{peak} evolution from the KW time-resolved spectral analysis (circles). Spectra at four major emission peaks in the KW light curve are marked: P1 (spectrum 5), P2 (spectrum 13), P3 (spectrum 21), and P4 (spectrum 26). The best power-law approximation from T_0 to $T_0 + 20$ s is shown with the solid line ($E_{\text{peak}}(t) \propto t^{-0.6}$).

low-energy photon index, α , indicates a spectrum enriched by higher-energy photons. Spectrum 5 describes the culmination of the pulse ($T_0 + 0.256$ – $T_0 + 0.512$ s). At this time, E_{peak} remains above 1 MeV and the energy flux, averaged over 256 ms, reaches a huge value of $\sim 7.8 \times 10^{-4}$ erg cm $^{-2}$ s $^{-1}$. The falling edge of the initial pulse (spectra 6–10, $T_0 + 0.512$ – $T_0 + 2.304$ s) is described by the further decrease in E_{peak} down to ~ 260 keV and by a slightly time-delayed steepening of α to ~ -1.3 .

At the peak rate, no obvious high-energy cutoff was observed up to the instrument’s upper energy threshold (Figure 7). For the initial 64 ms spectra 1 and 2 taken individually, the high-energy photon index, β , is poorly constrained. However, after applying a minimal time-averaging, the fit to the average spectrum 1+2 yields $\beta = -2.35^{+0.32}_{-0.79}$, consistent with the indices obtained for the subsequent spectra 3, 4, 5 and 6. Thus, no significant spectral variation is observed above several MeV during the onset and the culmination of the initial pulse. This result is illustrated by plot 7 in Figure 8, where photon light curves for different energy ranges are shown as constructed from the unfolded spectra. From this figure, one can see that the MeV emission decays dramatically with the decay of the initial pulse and has almost ceased after $\sim T_0 + 5$ s.

As already mentioned when discussing the KW light curves and their hardness ratio behavior, a correlation between the radiation intensity and its hardness is notable for the whole history of the burst. Onsets of all four major emission pulses are characterized by an apparent rise in E_{peak} and by a pronounced flattening of the low-energy part of the spectrum, with an opposite pattern in the decaying emission phases. At the same time, there is a clear trend of spectral softening from pulse to pulse: the top value of E_{peak} reached during each of the four major emission pulses steadily declines in time from ≈ 4 MeV for the initial pulse to ≈ 380 keV, ≈ 130 keV, and ≈ 105 keV for pulses P_2 , P_3 , and P_4 , respectively. The

general trend of the peak energy evolution in the prompt emission phase can be roughly described by a power-law slope $E_{\text{peak}}(t) \propto t^{-0.6}$ (Figure 9).

The behavior of the high-energy photon index, β , is consistent with the general tendency of the emission softening: β steepens, displaying weak variations, from ≈ -2.3 at the onset of the burst to $\beta \leq -3$ soon after the onset of Phase II and later.

2.2.5. Time-averaged Spectra and Energetics in the Prompt Emission

We analyzed the time-averaged spectrum of the entire prompt phase of the emission and its separate parts in the same way as described in the previous section. Among the tested models, the Band function is the only model that adequately describes the shape of the spectrum. The results of the fits are summarized in Table 4.

It should be emphasized that, having $E_{\text{peak}} \approx 340$ keV, $\alpha \approx -1.6$, and $\beta \approx -2.3$, the overall time-integrated spectrum (T_0 to $T_0 + 28.416$ s) is, indeed, the “average” one and does not reflect the spectral composition of the emission at any particular phase of the burst. As expected from the time-resolved spectral analysis, the average spectra of the first ($T_0 - T_0 + 13.312$ s, Phase I) and the second ($T_0 + 13.312 - T_0 + 28.416$ s, Phase II) pairs of overlapping pulses are essentially different. With only the low-energy photon index being close, $\alpha \simeq -1.2$, the peak energy differs between these phases of the burst almost by an order of magnitude ($E_{\text{peak}} \approx 630$ keV and ≈ 78 keV, respectively). Also, the high-energy photon index of the time-averaged spectrum is substantially softer in Phase II than in Phase I ($\beta \approx -3.3$ and $\beta \approx -2.3$, respectively). The average spectrum of the initial pulse ($T_0 - T_0 + 2.304$ s) is very hard: $E_{\text{peak}} \approx 1$ MeV, $\alpha \approx -1$, and $\beta \approx -2.4$.

Based on the results of the spectral and temporal analysis, we calculated the time-integrated and peak energy flux of the prompt γ -ray emission of GRB 110918A. In the 20 keV–10 MeV band, which is standard for Konus-WIND, the total energy fluence, S , from T_0 to $T_0 + 28.416$ s, is $(7.8 \pm 0.5) \times 10^{-4}$ erg cm $^{-2}$. More than half of this energy ($\sim 55\%$) is released in the initial pulse, $\sim 80\%$ during the hard Phase I, and only $\sim 1/5$ of the total fluence comes from the much softer Phase II.

The 64 ms peak energy flux, $F_{\text{max}} = (9.2 \pm 0.4) \times 10^{-4}$ erg cm $^{-2}$ s $^{-1}$, is reached in the interval starting 0.384 s after the trigger, at the culmination of the initial pulse (see Figure 4). As for the exceptionally high count rate, the F_{max} is the highest among >2000 GRBs detected by Konus-WIND so far. The 64-ms peak flux for Phase II is found to be ~ 20 times lower, $(4.5 \pm 0.5) \times 10^{-5}$ erg cm $^{-2}$ s $^{-1}$, in the interval starting at $T_0 + 17.536$ s, at the peak of the last, softest pulse in the light curve.

2.3. Extended Emission in γ -rays

It can be seen from the entire time history recorded by Konus-WIND (Figure 10) that the extremely bright pulsed phase of GRB 110918A ends ~ 30 s after the trigger. However, a stable excess in the count rate over the background level was detected by the instrument until the end of the measurements at $T_0 + 250$ s.

At this final phase of the γ -ray emission, the light curve shows a smooth temporal decay with a photon

Table 4
Konus-*WIND* Time-averaged Spectral Fits with the Band Function

Interval from T_0 (s)	α	β	E_{peak} (keV)	χ^2/dof	Fluence ^a ($10^{-4}\text{erg cm}^{-2}$)
0.000–28.416	$-1.64^{+0.06}_{-0.05}$	$-2.25^{+0.09}_{-0.09}$	340^{+70}_{-60}	77.5/81	$7.78^{+0.46}_{-0.45}$
0.000–2.304 (Initial pulse)	$-0.95^{+0.05}_{-0.05}$	$-2.41^{+0.10}_{-0.12}$	990^{+100}_{-90}	103/80	$4.03^{+0.11}_{-0.11}$
0.000–13.312 (Phase I)	$-1.12^{+0.08}_{-0.08}$	$-2.28^{+0.08}_{-0.10}$	630^{+160}_{-100}	54.4/81	$6.09^{+0.34}_{-0.38}$
13.312–28.416 (Phase II)	$-1.2^{+0.2}_{-0.1}$	$-3.3^{+0.2}_{-0.2}$	78^{+3}_{-3}	86.2/83	$1.57^{+0.33}_{-0.27}$

^a In the 20 keV–10 MeV energy band.

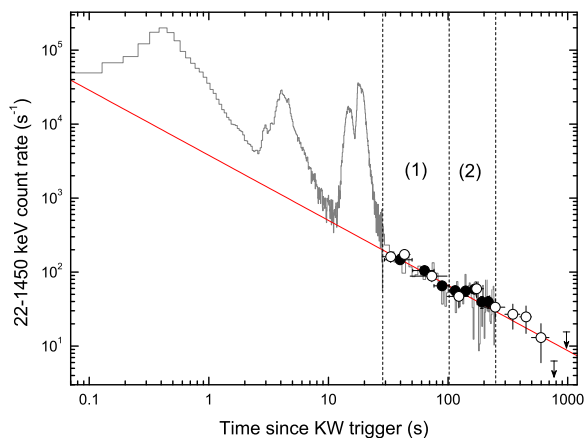


Figure 10. Prompt and extended phases of the GRB 110918A γ -ray emission (Section 2.3). Gray solid line: Konus-*WIND* count rate with 64 ms resolution before $T_0 + 28$ s and 2.944 s later). Time-averaged KW and SPI-ACS data after $T_0 + 28$ s, are shown by filled and open circles, respectively; the SPI-ACS counts are normalized to the KW counts in the 22–1450 keV energy range. The straight solid line shows the best power-law fit to the extended emission light curve, $N(t) \propto t^{-0.88 \pm 0.05}$; the ‘bump’ around $T_0 + 165$ s has been discarded to derive the best fit value. Time intervals (1) and (2) between the vertical dashed lines are used for the KW late-time spectral fits.

flux several orders of magnitude fainter and a substantially changed spectrum shape, as compared to the prompt phase. The “transitional” spectrum 35 (from $T_0 + 20.224$ s to $T_0 + 28.416$ s) is the last one which requires a “curved” spectral model in the fits. The subsequent time-resolved spectra were measured by KW out to $T_0 + 102.144$ s. Since the emission is weak, the individual spectra have poor signal-to-noise ratio, but may be adequately described by a simple power-law (PL) $f(E) \propto E^{-\Gamma}$, with a photon index, Γ , of 1.7–2.3. The average spectrum from $T_0 + 28.416$ s to $T_0 + 102.144$ s (interval 1 in Figure 10) extends to ~ 9 MeV and is best fit by a simple power law with $\Gamma = 2.00 \pm 0.12$ (1σ errors hereafter in this section) and $\chi^2 = 106/99$ d.o.f. The final portion of the KW data for GRB 110918A is avail-

able from the background mode light curves, which are measured out to $T_0 + 250$ s (interval 2 in the same figure). The time histories recorded in the G1, G2, and G3 energy bands are, in effect, a continuous three-channel spectrum covering the 22–1450 keV energy range. The power-law fit to the average three-channel spectrum from $T_0 + 100$ s to $T_0 + 250$ s yields $\Gamma = 2.18 \pm 0.24$ ($\chi^2 = 0.40/1$ d.o.f.), suggesting that there is no spectral evolution from the preceding interval 1, for which the same method gives $\Gamma = 1.96 \pm 0.13$ ($\chi^2 = 0.96/1$ d.o.f.); this is consistent with the index obtained for the multi-channel spectrum.

In the *INTEGRAL* SPI-ACS data (~ 80 keV–10 MeV energy band), the γ -ray emission of GRB 110918A can be traced to $\sim T_0 + 700$ s, after which the source flux becomes indistinguishable from the unstable background. Although the energy responses of the KW and SPI-ACS detectors are quite different, the stable power-law shape of the spectrum allowed us to extend the late-time γ -ray light curve beyond the end of the KW observation (open symbols in Figure 10). To ensure the correctness of the extrapolation, we normalized the count rate between the two instruments using counts accumulated in the interval from $T_0 + 50$ to $T_0 + 250$ s, well beyond the cessation of the prompt emission. For this interval the KW three-channel spectral fit yields $\Gamma = 2.00 \pm 0.16$ ($\chi^2 = 0.51/1$ d.o.f.); in the following analysis we assume this slope and the corresponding spectral index, $\beta_\gamma \equiv \Gamma - 1 = 1.00 \pm 0.16$, for the extended γ -ray emission.

A temporal power-law (PL) fit to the combined light curve, $N(t) \propto t^{-\alpha}$, yields, in the $T_0 + 30$ s– $T_0 + 700$ s time interval, the decay index $\alpha_\gamma = 0.84 \pm 0.05$ ($\chi^2 = 19.1/15$ dof). A count rate excess over this slope is found around $T_0 + 165$ s. Since the “bump” is present at the $\sim 2\sigma$ level in both KW and SPI-ACS data, it is unlikely to be a simple count rate fluctuation. Excluding the corresponding KW and SPI-ACS data points from the fit results in a better $\chi^2 = 10.8/13$ d.o.f., while the temporal index changes only marginally to $\alpha_\gamma = 0.88 \pm 0.05$ (the solid line in Figure 10).

Traced back in time, this slope lies just below the count rate observed at the KW light curve minimum around $T_0 + 11$ s, which may suggest that the power-law component emerges before the rise of Phase II of the prompt emission. A power-law fit to a three-channel spectrum constructed for the narrow time interval from $T_0 + 9.728$ s

to $T_0 + 11.776$ s yields $\Gamma = 2.01 \pm 0.03$ ($\chi^2 = 0.27/1$ d.o.f.), thus favoring this hypothesis.

Assuming a power-law spectrum with $\Gamma=2$, we estimate the 22–1450 keV energy fluence of the GRB 110918A extended emission from $T_0 + 28.416$ s to $T_0 + 700$ s to be $(2.6 \pm 0.5) \times 10^{-5}$ erg cm $^{-2}$, or $\approx 0.3\%$ of the energy in the prompt phase of the burst.

2.4. *Swift* Afterglow Observations

2.4.1. *Swift*/XRT Observations

The GRB 110918A IPN error box was observed by the *Swift* X-ray Telescope (XRT; Burrows et al. 2005) with tiling strategy starting ~ 83.0 ks after the KW trigger. No X-ray point source was detected in the very first observation. An unidentified X-ray source was detected close to the edge of the XRT field of view (FOV) in the first two snapshots of the second observation (starting ~ 107.4 ks after the trigger) and interpreted as the likely X-ray afterglow counterpart of GRB 110918A (Mangano et al. 2011a). Subsequent pointed observations of this source revealed a power-law decay of the flux and confirmed it as the counterpart (Mangano et al. 2011b). The best XRT position of the source is the UVOT-enhanced position (calculated using the XRT-UVOT alignment and by matching the UVOT field sources to the USNO-B1 catalogue): R.A.(J2000) = 32 $^{\circ}$ 53869 (02 h 10 m 9.29 s) decl.(J2000) = -27° 10576 (-27° 06'20.7") with an uncertainty of 1.4" (radius, 90% confidence). The refined IPN ellipse (Section 2.1) encompasses the counterpart.

Table 5 reports the log of the *Swift*/XRT observations used for this work. The source was observed by *Swift*/XRT in full frame Photon Counting mode (pcw3) for a total of 48 days and a total on-source exposure of ~ 280 ks in 2011, and 9 days with on-source exposure of ~ 20.5 ks one year later starting on October 4th in 2012 (see Section 2.4.4).

2.4.2. XRT Light Curve

The *Swift*/XRT count rate light curve in the 0.3–10 keV band has been built according to the light curve creation procedure described in Evans et al. (2007), requiring a minimum of 70 counts per bin and dynamic binning. In the 2012 observations, the source was not detected and only a 3σ upper limit of 1.28×10^{-3} counts s $^{-1}$ has been calculated using the Bayesian method of Kraft et al. (1991). The best-fit model is a single power law with decay slope $\alpha_X = -1.63 \pm 0.02$ and $\chi^2 = 46.4/45$ d.o.f. The count-rate light curve, together with best-fit model and residuals, is shown in Figure 11.

We tested the XRT afterglow light curve for the presence of a temporal break by fitting the data with a broken power law (BPL) function:

$$N(t) \propto \begin{cases} t^{-\alpha_1} & , (t < t_b) \\ t_b^{(\alpha_2 - \alpha_1)} t^{-\alpha_2} & , (t > t_b) \end{cases} \quad (2)$$

where t_b is the time of break in the light curve; α_1 and α_2 are the temporal indices before and after the break, respectively. An F -test shows that there is little evidence of an improvement in the fit if a break is added ($F = 4.62$, giving a null-hypothesis probability of 0.015). This result

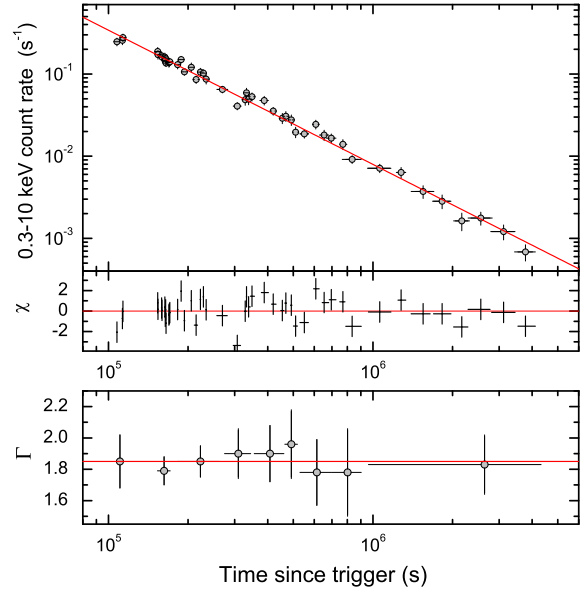


Figure 11. Top panel: *Swift*/XRT count rate light curve (symbols) with the best power-law fit (solid line) and residuals. Bottom panel: temporal evolution of the photon index, Γ , of the time-resolved *Swift*/XRT spectra (symbols). The photon index of the time-integrated spectrum ($\Gamma = 1.85$) is shown for reference with the solid line.

has been checked using different binning criteria. We generally find an F -test probability of $> 10^{-2}$ suggesting, that a BPL model is not needed, with a high significance, to fit the light curve.

We also tested a smoothly broken power law (Granot & Sari 2002); it results in an ambiguous fit and does not constrain the break.

2.4.3. XRT Spectra

We extracted average spectra of the source and the background after merging all the 2011 observations (sequences from 00020186002 to 00020187051 in Table 5, covering times from ~ 107.3 ks to ~ 4.325 Ms after the trigger). For the source extraction region, we used the 15-pixel-radius circular region needed to remain within the XRT FOV in sequence 00020186002.

To perform time-resolved spectral analysis, we also extracted a set of nine source and background spectra with comparable statistics. The observations were grouped as shown in Table 5. The small source extraction region with 15 pixel radius was used for spectrum 1 (coming from the highly offset initial observation) and for spectrum 9, corresponding to the faintest state of the source. The other spectra have been extracted from a circular 30-pixel-radius region. All background spectra were extracted from the same region used for the average background spectrum.

The spectra were all fit with an absorbed power law model with two absorption components: Galactic absorption in the direction of the source fixed at the value of 0.168×10^{21} cm $^{-2}$ (Kalberla et al. 2005) and intrinsic absorption at the measured redshift of $z=0.984$. A solar

Table 5
Swift/XRT observations of GRB 110918A

Spectrum	Sequence	Start Time (UT)	End Time (UT)	Exposure
(1)	(2)	(yyyy-mm-dd hh:mm:ss)	(yyyy-mm-dd hh:mm:ss)	(s)
		(3)	(4)	(5)
—	00020186001 ^a	2011-09-19 20:30:55	2011-09-19 20:59:05	1675
1	00020186002 ^b	2011-09-20 03:16:34	2011-09-20 07:39:25	2598
2	00020187001	2011-09-20 16:01:31	2011-09-20 20:59:48	6925
3	00020187002	2011-09-21 00:03:19	2011-09-21 22:30:56	8342
4	00020187003	2011-09-22 01:45:13	2011-09-22 21:13:56	8191
5	00020187004	2011-09-23 00:12:46	2011-09-23 00:26:56	830
	00020187005	2011-09-23 06:36:46	2011-09-23 21:02:57	4671
	00020187006	2011-09-24 01:57:11	2011-09-24 05:20:57	2023
6	00020187007	2011-09-24 06:26:48	2011-09-24 21:23:58	6928
7	00020187008	2011-09-25 00:28:30	2011-09-25 19:39:57	6807
	00020187009	2011-09-26 00:32:23	2011-09-26 23:10:57	8863
8	00020187010	2011-09-27 00:09:44	2011-09-27 23:06:57	7271
	00020187011	2011-09-28 00:38:07	2011-09-28 18:30:56	7702
	00020187012	2011-09-29 00:46:15	2011-09-29 08:29:58	4566
9	00020187013	2011-09-30 00:22:28	2011-09-30 18:37:57	4450
	00020187014	2011-10-01 00:25:45	2011-10-01 15:01:55	5050
	00020187015	2011-10-02 03:43:33	2011-10-02 10:24:56	4864
	00020187016	2011-10-03 07:00:51	2011-10-03 12:04:56	4929
	00020187017	2011-10-04 00:59:57	2011-10-04 07:21:56	4518
	00020187018	2011-10-05 00:44:43	2011-10-05 18:59:56	4185
	00020187019	2011-10-06 02:24:07	2011-10-06 23:45:56	3673
	00020187020	2011-10-07 15:31:38	2011-10-07 22:19:56	4964
	00020187021	2011-10-08 12:11:36	2011-10-08 17:27:56	4899
	00020187022	2011-10-09 10:39:43	2011-10-09 15:31:18	414
	00020187023	2011-10-10 09:07:53	2011-10-10 13:00:57	5092
	00020187024	2011-10-11 09:33:12	2011-10-11 17:30:57	4884
	00020187025	2011-10-12 06:04:30	2011-10-12 22:47:56	4919
	00020187026	2011-10-13 00:07:46	2011-10-13 21:09:56	4786
	00020187027	2011-10-14 12:37:29	2011-10-14 22:56:57	5115
	00020187028	2011-10-15 07:54:36	2011-10-15 19:35:56	5208
	00020187029	2011-10-16 00:21:58	2011-10-16 22:55:24	4190
	00020187030	2011-10-17 11:29:47	2011-10-17 18:07:58	3565
	00020187031	2011-10-18 08:06:28	2011-10-18 18:12:56	5072
	00020187032	2011-10-19 14:50:41	2011-10-19 21:26:57	5466
	00020187033	2011-10-20 18:13:31	2011-10-20 23:19:56	4069
	00020187034	2011-10-21 10:22:09	2011-10-21 20:14:56	5040
	00020187035	2011-10-22 16:42:29	2011-10-22 21:37:05	3377
	00020187036	2011-10-23 07:11:17	2011-10-23 08:51:00	364
	00020187037	2011-10-24 13:41:17	2011-10-24 18:32:40	4064
	00020187038	2011-10-25 01:00:38	2011-10-25 07:42:57	5320
	00020187039	2011-10-26 07:31:17	2011-10-26 21:59:57	4553
	00020187040	2011-10-27 09:00:17	2011-10-27 19:04:57	4992
	00020187041	2011-10-28 13:53:20	2011-10-28 19:09:58	4904
	00020187042	2011-10-29 18:48:19	2011-10-29 19:13:56	1534
	00020187043	2011-10-30 10:51:12	2011-10-30 19:17:58	8031
	00020187044	2011-10-31 11:11:01	2011-10-31 20:56:56	8234
	00020187045	2011-11-01 09:21:36	2011-11-01 17:48:49	8079
	00020187046	2011-11-02 07:59:37	2011-11-02 22:44:58	8550
	00020187047	2011-11-03 07:46:52	2011-11-03 21:09:56	7655
	00020187048	2011-11-04 06:24:06	2011-11-04 18:02:57	8096
	00020187049	2011-11-04 16:05:13	2011-11-05 22:58:56	9796
	00020187050	2011-11-06 08:05:06	2011-11-06 23:03:56	9904
	00020187051	2011-11-07 08:14:23	2011-11-07 23:04:18	8695
—	00020187052	2012-10-04 07:44:32	2012-10-04 23:59:54	2675
—	00020187053	2012-10-09 11:43:27	2012-10-09 11:46:55	188
—	00020187054	2012-10-10 16:02:44	2012-10-10 22:48:55	3049
—	00020187055	2012-10-11 13:07:42	2012-10-11 23:07:55	5348
—	00020187056	2012-10-12 21:04:55	2012-10-13 19:59:54	9232

Note. — Column 1 lists the reference number of the spectrum extracted after merging the data of the observations within horizontal separators; sequences not used for spectral analysis are marked with a ‘—’. Column 2 lists the sequence numbers of all the *Swift*/XRT pointed observations of GRB 110918A. Columns 3, 4 and 5 give information about start and stop time in UT and net exposure (after reduction and cleaning) of all observations, respectively.

^a GRB 110918A was out of the XRT FoV.

^b GRB 110918A was detected close to the edge of the XRT FoV only during the initial two snapshots, for a total exposure of 1481 s.

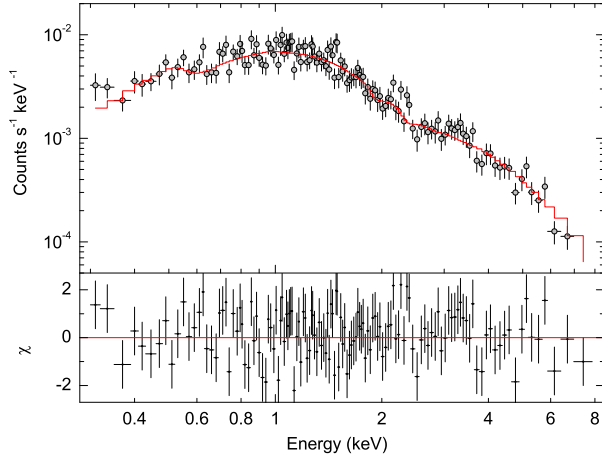


Figure 12. Average spectrum of the 2011 *Swift*/XRT observations together with the best-fit power-law model including Galactic and intrinsic absorption at the source and residuals (Section 2.4.3).

Table 6

Absorbed Power-law Fits to the Time-resolved *Swift*/XRT Spectra

Mean Epoch (ks from T_0)	Photon Index Γ	Observed Flux ($10^{-13} \text{erg cm}^{-2} \text{s}^{-1}$)	$\chi^2/\text{d.o.f.}$
111	$1.85^{+0.17}_{-0.17}$	$90.1^{+15.9}_{-12.4}$	7.64/9
162	$1.79^{+0.09}_{-0.09}$	$60.5^{+5.0}_{-4.3}$	36.7/41
223	$1.85^{+0.10}_{-0.10}$	$40.8^{+3.7}_{-2.9}$	33.5/34
310	$1.86^{+0.19}_{-0.18}$	$20.0^{+2.7}_{-2.4}$	21.6/17
408	$1.89^{+0.20}_{-0.19}$	$14.5^{+2.6}_{-1.9}$	7.37/11
491	$1.96^{+0.21}_{-0.22}$	$10.3^{+2.1}_{-1.5}$	8.56/8
613	$1.78^{+0.21}_{-0.21}$	$7.9^{+1.6}_{-1.2}$	11.9/12
802	$1.78^{+0.27}_{-0.28}$	$4.8^{+1.2}_{-0.89}$	12.7/10
2643	$1.83^{+0.18}_{-0.19}$	$0.78^{+0.13}_{-0.10}$	16.7/18

Note. — The flux is given in the (0.3–10) keV range. Galactic and intrinsic N_{H} at redshift $z=0.984$ have been fixed to $0.168 \times 10^{21} \text{cm}^{-2}$ and $2.33 \times 10^{21} \text{cm}^{-2}$, respectively.

metallicity is assumed for both absorption components.

The XRT average spectrum is best fit by an intrinsic absorption $N_{\text{H},i} = 2.33^{+0.58}_{-0.53} \times 10^{21} \text{cm}^{-2}$, a photon index $\Gamma = 1.85^{+0.07}_{-0.07}$ and $\chi_r^2 = 1.02$ (134 d.o.f.). The average [observed] unabsorbed flux in the 0.3–10 keV band is [5.3] $6.2 \times 10^{-13} \text{erg cm}^{-2} \text{s}^{-1}$. In Figure 12, we show the data and best fit model. From this fit we derived a rate to [observed] unabsorbed flux conversion factor in the 0.3–10 keV band of [4.58] $5.15 \times 10^{-11} \text{erg cm}^{-2}$.

The time-resolved spectra are all best fit with the same absorbed power law model. Fits performed with a free $N_{\text{H},i}$ parameter always lead to best-fit values consistent within errors with the ones previously obtained for the average spectrum. We then fixed $N_{\text{H},i}$ to $2.33 \times 10^{21} \text{cm}^{-2}$. Final results for the photon index, average observed flux, and χ_r^2 for the time-resolved spectra are listed in Table 6; the index is shown in the lower panel of Figure 11, where we see no evidence of spectral evolution.

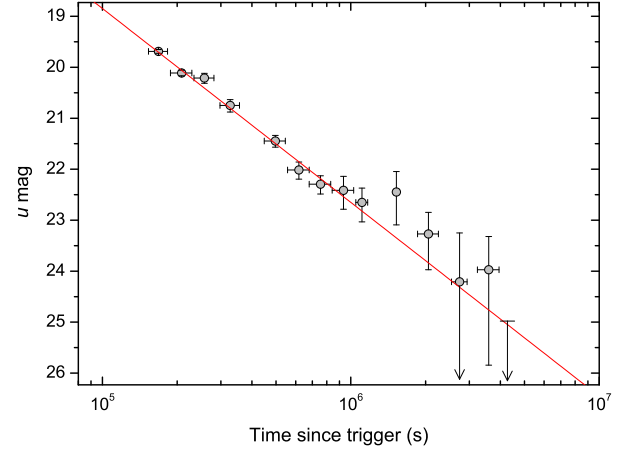


Figure 13. UVOT light curve of GRB 110918A afterglow (Table 7). The underlying galaxy flux is subtracted and the data are normalized to the count rate in the *u* filter. The solid line shows a best power-law fit with a slope of 1.52 ± 0.05 .

Table 7

UVOT Combined Normalized Photometry

T_{mid} (ks from T_0)	Half-exposure (ks)	Count Rate (s^{-1})	<i>u</i> (mag)
168.1	14.8	0.2895 ± 0.0099^a	$19.69^{+0.04}_{-0.04}$
208.5	20.7	0.1961 ± 0.0098	$20.11^{+0.06}_{-0.05}$
257.5	23.7	0.1788 ± 0.0160	$20.21^{+0.10}_{-0.09}$
326.8	29.6	0.1090 ± 0.0122	$20.75^{+0.13}_{-0.11}$
496.7	48.5	0.0574 ± 0.0061	$21.44^{+0.12}_{-0.11}$
618.2	61.8	0.0340 ± 0.0052	$22.01^{+0.18}_{-0.16}$
755.0	74.9	0.0263 ± 0.0043	$22.29^{+0.20}_{-0.17}$
933.8	92.8	0.0235 ± 0.0068	$22.41^{+0.37}_{-0.28}$
1108.7	61.2	0.0189 ± 0.0056	$22.65^{+0.38}_{-0.28}$
1525.1	38.5	0.0228 ± 0.0102	$22.45^{+0.64}_{-0.40}$
2054.1	197.7	0.0107 ± 0.0051	$23.27^{+0.70}_{-0.42}$
2741.1	197.1	0.0045 ± 0.0064	$24.20^{+nan}_{-0.98}$
3591.8	358.7	0.0056 ± 0.0046	$23.96^{+1.81}_{-0.65}$
4143.1	182.7	< 0.0022	> 24.98
33366.3	410.9	< 0.0034	> 24.51

^a 1σ errors in this table.

2.4.4. *Swift*-UVOT Observation and Analysis

Swift's Ultraviolet Optical Telescope (UVOT; Roming et al. 2000, 2004, 2005) began observing the burst approximately 153 ks after the KW trigger. Data were initially taken in UVOT's *white* filter, but late-time data (200–500 ks after the trigger) were also taken in UVOT's four ultraviolet filters (*u*, *uvw1*, *uvm2* and *uvw2*) until *Swift* ceased observations.

Photometry was measured with UVOTSOURCE using the calibrations of Poole et al. (2008), Breeveld et al. (2010), and Breeveld et al. (2011). A combined light curve from all detections, normalized to the count rate in the *white* filter, suggests a late-time flattening of the light curve. In order to exclude contamination from nearby sources or the possible host galaxy, we requested

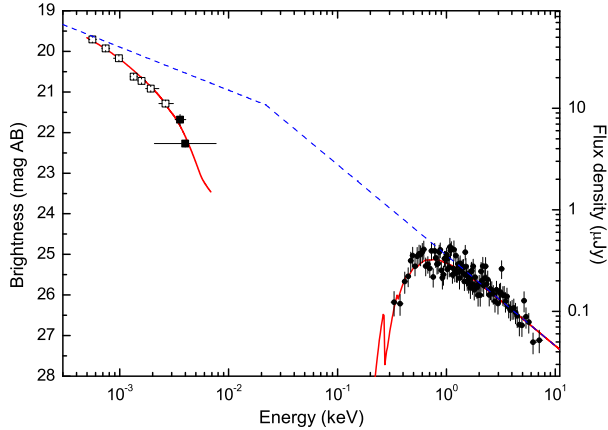


Figure 14. Broadband SED of GRB 110918A afterglow. The SED is built for an epoch at 300 ks after the trigger (Section 2.4.5) using the XRT spectra (solid circles), the UVOT photometry (solid squares), and the GROND host-subtracted photometric data from E13 (open squares). The best BPL fit for the SMC dust model is shown (solid line) together with the model corrected for extinction and absorption effects (dashed line). The break is located between the UVOT and XRT bands and the spectral slope change, $\beta_X - \beta_{\text{opt}} \approx 0.47$, is consistent with a cooling break of the standard fireball model.

additional observations with *Swift*/UVOT. Since the best coverage of the afterglow was in the *white* and *u* filters, we requested 10 ks of observations for each of these two filters. We examined these data for the presence of a host galaxy and, within the source aperture, we found a candidate object. Analysis of this object provided a 5.3σ detection in *white* with a magnitude of 22.63 ± 0.21 and a 2.6σ detection in the *u* band at a magnitude of 22.49 ± 0.42 (1σ errors). These findings are in agreement with E13, where results of detailed studies of the host can be found.

Using the late-time UVOT observations, we subtracted the underlying flux from the *white* and *u*-band data. Figure 13 and Table 7 show the combined light curve from these two bands, normalized to the *u* filter and co-added. The host-subtracted light curve shows a power-law decay with a slope $\alpha_{\text{opt}} = -1.52 \pm 0.09$ ($\chi^2 = 9.35/11$ d.o.f) out to 3.4 Ms after the trigger. Introducing a temporal break does not improve the fit: the best BPL fit yields $\chi^2 = 9.27/9$ d.o.f and a very high (96%) probability of chance improvement over the simple power law. The pre- and post-break indices $\alpha_1 = 1.46 \pm 0.19$ and $\alpha_2 = 1.55 \pm 0.16$ are indistinguishable within 1σ errors, and the break time, $t_b = 258 \pm 415$ ks, cannot be determined. A search for an achromatic break in the UV/optical and X-ray afterglow was performed by fitting the UVOT and XRT data with the BPL model simultaneously. We put minimal restrictions on the procedure and tied only the key model parameter, t_b , between the optical and the X-ray light curves. Nevertheless, no limits on the break were found in the fits and an F-test probability ≈ 0.09 suggests that the BPL law model is not needed.

2.4.5. Broadband SED

In a companion paper (E13), a broadband spectral energy distribution (SED) of the GRB 110918A after-

glow was studied, as constructed from the optical/NIR GROND photometry at a midtime of 194 ks, and the XRT data between 140 ks and 250 ks. From the best simple PL fit ($\chi^2 = 85/73$ d.o.f), the authors derived a line-of-sight extinction $A_V = 0.16 \pm 0.06^1$ mag, an intrinsic column density $N_{\text{H},i} = 1.56_{-0.46}^{+0.52} \times 10^{21} \text{ cm}^{-2}$, and a broadband spectral slope $\beta_{OX} = 0.70 \pm 0.02$; they also found that a BPL modeling of the SED does not improve the fit ($\chi^2 = 83/71$ d.o.f).

Using the GROND host-subtracted photometry from E13, we analyzed a broadband SED built following the method of Schady et al. (2010) from the GROND data in the $g'r'i'z'JHK_S$ bands, the XRT data, and the host-subtracted UVOT photometry in the *u* and *white* filters. The SED was constructed for an epoch centered at 300 ks utilizing the observations from 107 ks to 450 ks after the trigger. Fits were made in XSPEC with the absorbed power-law model and three dust extinction curves from Pei (1992): the Milky Way (MW) with $R_V = 3.08$, the Large Magellanic Cloud (LMC) with $R_V = 3.16$, and the Small Magellanic Cloud (SMC) with $R_V = 2.93$. The Galactic reddening is fixed to 0.02 mag (Schlegel et al. 1998) and the Galactic column density is set to $0.168 \times 10^{21} \text{ cm}^{-2}$. The best fit with a simple PL ($\chi^2 = 155.3/111$ d.o.f) is achieved for the SMC dust profile and closely reproduces the results of E13 at 194 ks: $A_V = 0.22 \pm 0.02$ mag, $N_{\text{H},i} = 1.65_{-0.38}^{+0.42} \times 10^{21} \text{ cm}^{-2}$, and $\beta_{OX} = 0.69 \pm 0.01$. This slope and the implied column density are in poor agreement with the ranges obtained in our analysis of both time-resolved and time-averaged XRT spectra; this suggests that a single PL does not describe the broadband SED adequately. As distinct from E13, a BPL model significantly improves our fit, with $\chi^2 = 128.4/109$ d.o.f. and a chance improvement probability over the simple PL of 3.1×10^{-5} . The best BPL fit (Figure 14) is found for the same SMC dust profile; it yields $A_V = 0.35 \pm 0.09$ mag, $N_{\text{H},i} = 2.94_{-0.66}^{+0.73} \times 10^{21} \text{ cm}^{-2}$, the break energy $E_b = 0.022_{-0.013}^{+0.046} \text{ keV}$, $\beta_{\text{opt}} = 0.42 \pm 0.18$, and $\beta_X = 0.89_{-0.07}^{+0.08}$. This result is in agreement with the XRT spectral analysis and a spectral slope change $\beta_X - \beta_{\text{opt}} \approx 0.47$ suggests a cooling break between the UVOT and XRT spectral bands; the derived range of E_b favors of this hypothesis.

The XRT+UVOT+GROND SED centered at 194 ks (the E13 epoch) was also tested and we found that both simple and broken PL fits result in a 1σ agreement with those for the SED at 300 ks. Thus, the significant improvement found for the BPL fits in this work may result from a combination of at least two factors. First, with the UVOT observations added, the shape of the optical part of the SEDs at both epochs is better understood. Second, the overall signal-to-noise ratio in the SED at 300 ks is considerably higher, since it was built from the ~ 3.5 -times longer time span of observations.

We note that $A_V \sim 0.35$ derived from the BPL fit is higher than the line-of-sight extinction resulting from a simple PL, but still much smaller than the average A_V of the host galaxy's starlight (~ 0.90 mag) reported by E13. This inconsistency has been discussed in E13; the authors consider two explanations: (1) a clumpy geometry of dust within the host and (2) that the progenitor had

¹ E13 reported errors at the 1σ confidence level.

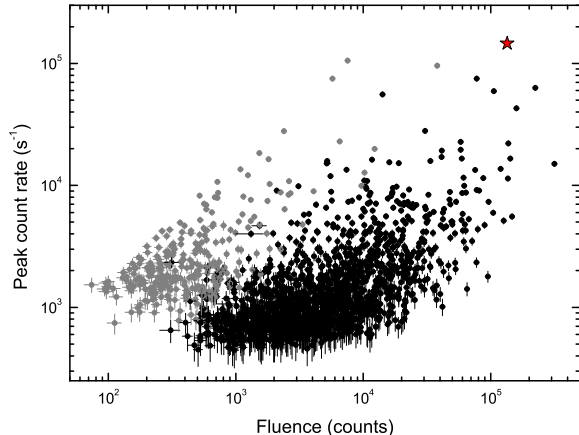


Figure 15. Peak count rate vs. total recorded counts for 1834 Konus-*WIND* GRBs detected in 1994–2010 (Svinkin et al., in preparation): 1560 long (dark circles) and 274 short duration (gray circles); GRB 110918A is indicated by the star. The counts are in the Konus-*WIND* G2+G3 energy band; the peak count rate is measured over 64 ms.

enough time to destroy local dust with its UV emission. Bearing in mind the huge brightness of GRB 110918A, the latter option can be naturally extended by the possibility that the GRB itself partially destroyed dust grains along the line of sight (see, e.g., Waxman & Draine 2000; Fruchter et al. 2001).

3. DISCUSSION

3.1. GRB 110918A in the Cosmological Rest Frame

Konus-*WIND* started operation in 1994 November, and, in almost 19 years, has detected more than 2000 γ -ray bursts, with virtually no bright GRBs having been missed. Among these bursts, GRB 110918A is, without a doubt, an outstandingly bright event (Figure 15). Its fluence, both in energy and count spaces, is among the half-dozen highest observed. The burst’s 64 ms peak count rate is unprecedented. Its peak energy flux is surpassed only on the short 2 ms timescale by the two ultra-bright, short, hard bursts GRB 051103 and GRB 070201, the candidate giant flares from soft γ -ray repeaters in the nearby galaxies M81/82 and M31 (Frederiks et al. 2008; Mazets et al. 2008; Hurley et al. 2010).

The huge energy flux measured by KW suggests an enormous energy released in the cosmological rest frame. Assuming a redshift of $z = 0.984$ and a standard cosmology model with $H_0 = 71 \text{ km s}^{-1} \text{ Mpc}^{-1}$, $\Omega_M = 0.27$, and $\Omega_\Lambda = 0.73$, the luminosity distance D_L is $2.0 \times 10^{28} \text{ cm}$. Derived from the total energy fluence and the peak energy flux (Section 2.2.5), the isotropic-equivalent energy release in γ -rays, E_{iso} , is $(2.1 \pm 0.1) \times 10^{54} \text{ erg}$, and the peak isotropic luminosity, L_{iso} , is $(4.7 \pm 0.2) \times 10^{54} \text{ erg s}^{-1}$ (both quantities are in the rest-frame 1–10000 keV band).

These estimates make GRB 110918A one of the most energetic and the most luminous γ -ray burst observed since the beginning of the cosmological era in 1997. Figure 16 shows E_{iso} and L_{iso} for GRB 110918A along with almost one hundred KW GRBs with known redshifts; this sample is discussed in detail by Tsvetkova

et al. (in preparation), hereafter T13. One can see that GRB 110918A lies at the upper edge of the E_{iso} distribution and is nearly an order of magnitude more luminous than any burst at $z \sim 1$.

In Figure 16, the KW detection horizon for a GRB 110918A-like event is also indicated. The limit of $z \sim 7.5$ is estimated by applying the KW triggering algorithm to simulated light curves at different redshifts. The simulations, which account for both time dilation and spectral reddening, show that at $z \geq 5$, only the initial pulse remains detectable in the KW band; at high redshifts the burst is seen as a short ($T_{90} \sim 2 - 3 \text{ s}$) GRB with moderate $E_{\text{peak}} \sim 300 \text{ keV}$ and relatively long spectral lag of $\sim 200 \text{ ms}$. Assuming a *Swift*/BAT sensitivity of $10^{-8} \text{ erg cm}^{-2} \text{ s}^{-1}$ in the 15–150 keV band (Barthelmy et al. 2005), its detection threshold is reached at $z \sim 12$.

The key rest-frame parameters of GRB 110918A, the intrinsic peak energy, $E_{p,i} \equiv E_{\text{peak}}(1+z) = 670 \pm 140 \text{ keV}$, and the rest-frame duration, $T_{90}/(1+z) = 9.9 \pm 0.05 \text{ s}$, are nearly at the center of the distributions for the KW sample and may be considered typical. Consequently the huge energetics of GRB 110918A cannot be easily explained by an extremely hard spectrum or by long-lasting prompt emission. Since more than half of the burst’s energy is released in the hard initial pulse (Section 2.2.5), the intrinsic peak energy of the pulse’s time-averaged spectrum ($2000 \pm 200 \text{ keV}$) is also an important characteristic of the event. It is in the top 10% of the KW $E_{p,i}$ distribution, but it cannot be the sole reason for the GRB 110918A record energy. Therefore, the most likely explanation for both the observed and isotropic-equivalent rest-frame energetics is a huge photon flux, which suggests a highly-collimated emission.

We tested the GRB 110918A rest-frame characteristics against $E_{p,i} - E_{\text{iso}}$ and $E_{p,i} - L_{\text{iso}}$ relations—known as the “Amati” and “Yonetoku” correlations (Amati et al. 2002; Yonetoku et al. 2004, respectively; we used their recent updates from Ghirlanda et al. 2012). One can see from Figure 17 that the burst is close to being a luminous outlier with respect to both relations, suggesting that the spectral hardness of GRB 110918A is likely a minor ingredient of the burst’s isotropic energy as compared to the population. On the other hand, the spread in the spectral-energy correlations is known to diminish when the jet effect is taken into account (Ghirlanda et al. 2004, 2007); this supports the hypothesis that the GRB 110918A collimation is relatively tighter when compared to an average GRB. It should be noted, finally, that the initial pulse taken alone follows the $E_{p,i} - E_{\text{iso}}$ relation to within 1σ and the $E_{p,i} - L_{\text{iso}}$ relation to within $\sim 1.5\sigma$. This is particularly important since, as mentioned above, the initial pulse is the only phase of the burst which could be seen from high redshifts and emphasizes the role of observational bias in these studies.

3.2. Bulk Lorentz Factor of the Ejecta

Several methods have been proposed to estimate the bulk Lorentz factor of the GRB ejecta (Γ_0): the pair-opacity constraint from the “compactness” problem (Lithwick & Sari 2001), the optical afterglow onset method (e.g., Sari & Piran 1999), and the very early external shock emission method, which consid-

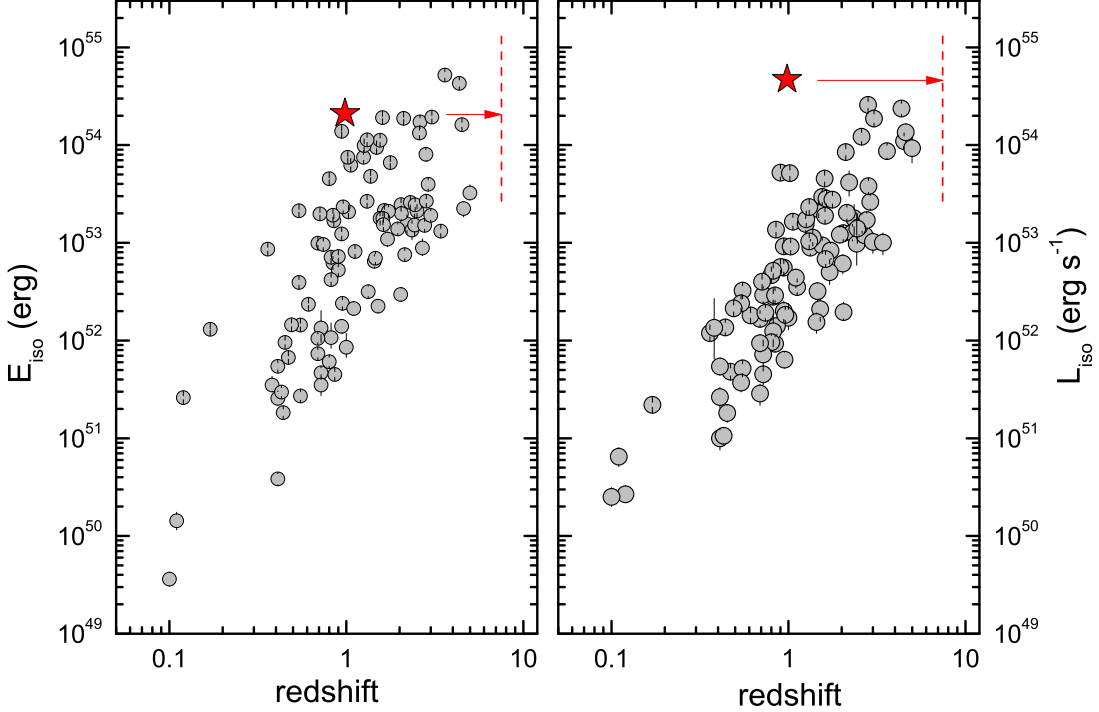


Figure 16. E_{iso} (left) and L_{iso} (right) of GRB 110918A (stars) and Konus-*WIND* GRBs with known redshifts. The gray circles show data for the KW bursts from Tsvetkova et al. (in preparation). The dashed lines indicate the KW detection horizon for a GRB 110918A-like burst ($z \sim 7.5$).

ers the quiescent periods between the prompt emission pulses (Zou & Piran 2010). Since no early observations are available for the GRB 110918A afterglow and the prompt emission pulses overlap considerably, only the first method mentioned is applicable.

We calculated the lower limit on Γ_0 using inequalities from Lithwick & Sari (2001). The first (Limit A) is

$$\Gamma_{0,A} > \hat{\tau}^{1/(2\beta+2)} (E_{\text{max}}/m_e c^2)^{(\beta-1)/(2\beta+2)} (1+z)^{\beta-1/\beta+1}; \quad (3)$$

and the second (Limit B) is

$$\Gamma_{0,B} > \hat{\tau}^{1/(\beta+3)} (1+z)^{\beta-1/\beta+3}, \quad (4)$$

where β is the photon power-law index at MeV energies (in the $N(E) \propto E^{-\beta}$ notation), E_{max} is the highest energy at which photons were observed, and

$$\hat{\tau} \simeq 4.3 \times 10^{10} \frac{f_1}{\beta-1} D_{L,28}^2 0.511^{1-\beta} (\delta T/0.1)^{-1}, \quad (5)$$

where δT is the minimum variability time scale of the prompt emission, and f_1 is the photon flux at 1 MeV.

From the KW analysis, we assume the following parameters for GRB 110918A: $\delta T=0.25$ s, $\beta = 2.39$, $E_{\text{max}} > 18$ MeV, and $f_1 = 160 \text{ cm}^{-2} \text{ s}^{-1} \text{ MeV}^{-1}$, all taken at the peak of the initial pulse (see Sections 2.2.3 and 2.2.4). This yields $\Gamma_{0,A} > 240$ and $\Gamma_{0,B} > 360$; by applying the tighter limit, we conclude $\Gamma_0 > 360$.

Typically, when photons are observed at high energies ($E_{\text{max}} \sim \text{GeV}$), Limit A yields a stricter constraint than Limit B. Unfortunately, GRB 110918A was not observed by high-energy missions and we proceeded from a very conservative Konus-*WIND* limit, $E_{\text{max}} > 18$ MeV. However, the value of $\Gamma_{0,B}$ allows us to set the lower limit on the high-energy cutoff of the GRB 110918A emission spectrum to $E_{\text{max}} \geq 100$ MeV (assuming that the spectrum measured by Konus-*WIND* in the MeV band extends unchanged to those energies).

Liang et al. (2010) discovered a tight correlation between Γ_0 and E_{iso} . This correlation was confirmed and refined on a broader GRB sample by Lü et al. (2012) who obtained $\Gamma_0 \simeq 91 E_{\text{iso},52}^{0.29}$. In the latter work, another tight correlation between Γ_0 and L_{iso} was found in the form of $\Gamma_0 \simeq 249 L_{\text{iso},52}^{0.30}$. Applied to GRB 110918A these relations yield Γ_0 values of 430 and 1580, respectively. Close values ($\Gamma_0(E_{\text{iso}}) \sim 450$ and $\Gamma_0(L_{\text{iso}}) \sim 1450$) are evaluated based on slightly different slopes from Ghirlanda et al. (2012). It should be noted, however, that the GRB samples used by Lü et al. (2012) and Ghirlanda et al. (2012) do not contain any burst with $\Gamma_0 > 1000$ or $L_{\text{iso}} > 10^{54} \text{ erg s}^{-1}$, which is the case for this burst. Thus, the Γ_0 value of ~ 450 obtained from the $\Gamma_0 - E_{\text{iso}}$ relation, which is tested by both authors up to $E_{\text{iso}} \sim 10^{54}$ erg, may be considered more feasible than $\Gamma_0 \sim 1500$ derived from L_{iso} . The Γ_0 estimate of a

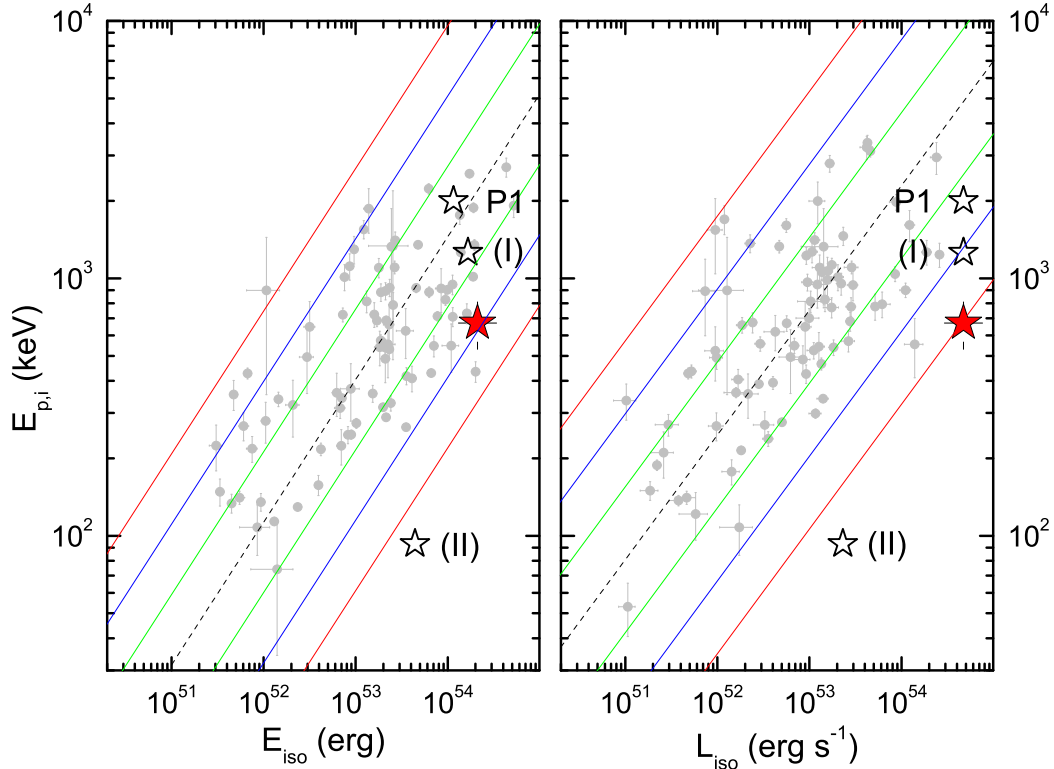


Figure 17. Rest-frame energetics in the $E_{\text{iso}} - E_{\text{p},i}$ (left) and $L_{\text{iso}} - E_{\text{p},i}$ (right) planes. GRB 110918A is shown with filled stars; the open symbols show Phase I (I), Phase II (II), and the initial pulse alone (P1). The KW GRBs with known redshifts are shown with gray symbols. The recent updates for the Amati ($E_{\text{p},i} - E_{\text{iso}}$) and Yonetoku ($E_{\text{p},i} - L_{\text{iso}}$) relations from Ghirlanda et al. (2012) are plotted with the dashed lines together with their 1σ , 2σ , and 3σ scatters (solid lines).

few hundred is supported by another correlation studied by Ghirlanda et al. (2012), the $\Gamma_0 - E_{\text{p},i}$ relation. From $E_{\text{p},i} = 670$ keV, this relation yields $\Gamma_0 = 150$ and, from $E_{\text{p},i} = 2000$ keV for the initial pulse, $\Gamma_0 = 400$.

3.3. Scenarios for Afterglow and Extended γ -ray Emission

In Section 2.3, it was shown that at ~ 30 s after the KW trigger, the prompt phase of GRB 110918A rapidly developed into a steadily decaying “tail” of the extended γ -ray emission. The decay follows a power law with the temporal index $\alpha_\gamma \approx 0.88$ out to $\sim T_0 + 700$ s. At the same time, the emission spectrum is well described by a power law with spectral index $\beta_\gamma \approx 1$. The combination of the spectral and temporal behavior is in fairly good agreement with that expected at the “plateau” (II) and “normal” (III) phases of the canonical X-ray afterglow (Nousek et al. 2006; Zhang et al. 2006). This supports a scenario in which the extended γ -ray emission of GRB 110918A is generated by the synchrotron forward-shock mechanism with a possible late-time energy injection.

Swift observations of the GRB 110918A afterglow started ~ 107 ks after the burst and showed no clear

signature of a possible jet break in the X-ray and UV/optical light curves up to the time the observations ceased ~ 48 days later. The XRT temporal slope, $\alpha_X \approx 1.63$, cannot be unambiguously attributed to the “normal” (III) or “jet” (IV) segment of the canonical X-ray afterglow; α_X is at the steep end of the segment III indices and at the shallow end of the segment IV indices for a sample of XRT afterglows with “prominent” jet breaks (Racusin et al. 2009). The slope of 1.5, which is widely suggested as critical to distinguish the pre-break and post-break segments of both X-ray and optical afterglows (see, e.g., Panaitescu (2007), Liang et al. (2008)), is also too close to α_X and $\alpha_{\text{opt}} \approx 1.52$ to draw any firm conclusion. Thus the question of the jet break location with respect to the time span of the *Swift* observations cannot be easily answered when discussing the afterglow temporal slopes alone.

The standard fireball model for GRB afterglows suggests that their temporal α , and spectral β , indices follow closure relations (CRs), which are linear relationships between α and β , both being linear functions of a power-law index of the underlying electron spectrum p . We tested the GRB 110918A observations against an extensive set of CRs collected

Table 8
Closure Relations

Geometry	Medium	Spectral Regime	p	α_{cr}	f_{cr}	CR	Reference
Extended γ -ray emission ($\alpha_{\text{obs}} = 0.88 \pm 0.05$, $\beta_{\text{obs}} = 1.00 \pm 0.16$)							
<i>SE</i>	<i>ISM</i>	$\nu_\gamma < \nu_c$	3.0 ± 0.3	1.5	3.3σ	$\alpha = 3\beta/2$	1a
<i>SE</i>	<i>Wind</i>	$\nu_\gamma < \nu_c$	3.0 ± 0.3	2.0	6.0σ	$\alpha = (3\beta + 1)/2$	5a
<i>SE</i>	<i>ISM, Wind</i>	$\nu_c < \nu_\gamma$	2.0 ± 0.3	1.0	0.6σ	$\alpha = (3\beta - 1)/2$	2a, 6a
XRT ($\alpha_{\text{obs}} = 1.63 \pm 0.02$, $\beta_{\text{obs}} = 0.85 \pm 0.04$)							
<i>SE</i>	<i>ISM</i>	$\nu_X < \nu_c$	2.7 ± 0.1	1.28	5.6σ	$\alpha = 3\beta/2$	1a
<i>SE</i>	<i>Wind</i>	$\nu_X < \nu_c$	2.7 ± 0.1	1.83	2.3σ	$\alpha = (3\beta + 1)/2$	5a
<i>JET</i>	<i>ISM, Wind</i>	$\nu_X < \nu_c$	2.7 ± 0.1	2.70	13σ	$\alpha = 2\beta + 1$	9a
<i>JETns</i>	<i>ISM</i>	$\nu_X < \nu_c$	2.7 ± 0.1	2.03	6.2σ	$\alpha = (6\beta + 3)/4$	11a
<i>JETns</i>	<i>Wind</i>	$\nu_X < \nu_c$	2.7 ± 0.1	2.28	10σ	$\alpha = (3\beta + 2)/2$	13a
<i>SE</i>	<i>ISM</i>	$\nu_c < \nu_X$	1.7 ± 0.1	0.94	27σ	$\alpha = (3\beta + 5)/8$	2b
<i>SE</i>	<i>Wind</i>	$\nu_c < \nu_X$	1.7 ± 0.1	0.96	30σ	$\alpha = (\beta + 3)/4$	6b
<i>JET</i>	<i>ISM, Wind</i>	$\nu_c < \nu_X$	1.7 ± 0.1	1.93	10σ	$\alpha = (\beta + 3)/2$	10b
<i>JETns</i>	<i>ISM</i>	$\nu_c < \nu_X$	1.7 ± 0.1	1.69	2.5σ	$\alpha = (3\beta + 11)/8$	12b
<i>JETns</i>	<i>Wind</i>	$\nu_c < \nu_X$	1.7 ± 0.1	1.46	7.5σ	$\alpha = (\beta + 5)/4$	14b
UVOT ($\alpha_{\text{obs}} = 1.52 \pm 0.09$, $\beta_{\text{obs}} = 0.42 \pm 0.11$)							
<i>SE</i>	<i>ISM</i>	$\nu_{\text{opt}} < \nu_c < \nu_X$	1.8 ± 0.2	0.72	8.1σ	$\alpha = 3(2\beta + 3)/16$	1b
<i>SE</i>	<i>Wind</i>	$\nu_{\text{opt}} < \nu_c < \nu_X$	1.8 ± 0.2	1.23	3.1σ	$\alpha = (2\beta + 9)/8$	5b
<i>JET</i>	<i>ISM, Wind</i>	$\nu_{\text{opt}} < \nu_c < \nu_X$	1.8 ± 0.2	1.96	9.1σ	$\alpha = (2\beta + 7)/4$	9b
<i>JETns</i>	<i>ISM</i>	$\nu_{\text{opt}} < \nu_c < \nu_X$	1.8 ± 0.2	1.47	0.5σ	$\alpha = (6\beta + 21)/16$	11b
<i>JETns</i>	<i>Wind</i>	$\nu_{\text{opt}} < \nu_c < \nu_X$	1.8 ± 0.2	1.73	2.2σ	$\alpha = (2\beta + 13)/8$	13b

Note. — Column 1 is the outflow geometry and dynamics: *SE* (spherical expansion), *JET* (spreading jet), *JETns* (non-spreading jet). Column 2 is the circum-burst density profile $n(r) \propto r^{-s}$: *ISM* ($s = 0$), *Wind* ($s = 2$). Column 3 is the position of the observation band ν relative to the synchrotron cooling frequency ν_c ; the slow-cooling regime, $\nu_m < \min(\nu, \nu_c)$, is assumed. Column 4 is the electron spectral distribution index, given the spectral regime and β_{obs} . Column 5 is the CR-predicted temporal index α_{cr} . Column 6 is the deviation of the observed temporal index α_{obs} from α_{cr} . Column 7 is the closure relation and column (8) is its index in Table 1 of Racusin et al. (2009), where the references can be found.

in Table 1 of Racusin et al. (2009), which, in turn, are taken from Zhang & Mészáros (2004), Dai & Cheng (2001), Zhang et al. (2006), Panaitescu (2005), and Panaitescu et al. (2006). Following Zhang et al. (2006), we expect the typical synchrotron frequency, ν_m , to lie below the observational bands and, for the XRT and UVOT observations, which started ~ 107 ks after the burst, we assume the slow-cooling regime ($\nu_m < \nu_c$), where ν_c is the synchrotron-cooling frequency.

In Table 8, the values of $p(\beta_{\text{obs}})$ and the deviations $f_{\text{cr}} \equiv \alpha_{\text{cr}}(\beta_{\text{obs}}) - \alpha_{\text{obs}}$ are listed, where α_{cr} is the temporal slope predicted by the closure relation and the indices α_{obs} , β_{obs} , are obtained from our observations. Figure 18 shows the $\alpha(\beta)$ diagram for the closure relations and the data.

X-ray afterglow. In the $\nu_c < \nu_X$ regime, the electron index $p = 2\beta_X = 1.7 \pm 0.14$. From (α_X, β_X) and CRs for this spectral regime (Figure 18, right) a pre-break geometry of ejecta which mimics an isotropic, spherical expansion (SE), is rejected at $> 20\sigma$. The best-fitting CR (2.5σ) is for the non-spreading jet (JETns) and ISM-like circum-burst medium (CBM). Another option, the $\nu_X < \nu_c$ spectral regime, which is considered unlikely for late-time X-ray afterglows (see, e.g., Zhang et al. (2006); Nysewander et al. (2009)), yields a steep electron spectrum, $p = 2\beta_X + 1 = 2.7 \pm 0.14$. In this case, all the jet closure relations are $> 6\sigma$ from the X-ray observations; the best fitting CR suggests the pre-break (SE) geometry and a stellar-wind-like CBM (2.3σ).

UV/optical afterglow. The UVOT temporal slope, $\alpha_{\text{opt}} = 1.52 \pm 0.09$, is shallower but consistent with α_X . For the spectral slope in the optical band, we ac-

cept $\beta_{\text{opt}} = 0.42 \pm 0.11$ (1σ) obtained from the broadband XRT+UVOT+GROND SED in Section 2.4.5. The $\nu_c < \nu_{\text{opt}}$ regime implies an ultra-hard electron index of $p = 2\beta_{\text{opt}} = 0.84 \pm 0.22$, which is at odds with both values of p suggested from the X-ray spectrum. Alternatively, in the $\nu_{\text{opt}} < \nu_c$ regime $p = 2\beta_{\text{opt}} + 1 = 1.84 \pm 0.22$, which is in good agreement with the electron index found for $\nu_c < \nu_X$. In this case, a cooling break of $\Delta\beta = 1/2$ is expected between the UVOT and XRT bands, which is consistent with $\beta_X - \beta_{\text{opt}} = 0.43 \pm 0.12$. From $(\alpha_{\text{opt}}, \beta_{\text{opt}})$ all pre-break CRs are $> 3\sigma$ from the data and the JETns+ISM is again the best fitting CR (0.5σ).

Extended γ -ray emission. Given $\beta_\gamma = 1.00 \pm 0.16$ and $\alpha_\gamma = 0.88 \pm 0.05$, the fast-cooling regime $\nu_c < \nu_\gamma < \nu_m$, which requires $\beta = 1/2$ for the ISM and $\alpha = 0$ for the wind-like CBM, is ruled out at $> 3\sigma$. The same is true for the slow-cooling regime and $\nu_\gamma < \nu_c$ (see Figure 18, left panel). In the $\max(\nu_m, \nu_c) < \nu_\gamma$ regime, the electron index is $p = 2\beta_\gamma = 2.0 \pm 0.3$, which is consistent with $p \sim 1.7$, implied for $\nu_c < \nu_X$. The SE closure relation fits the observations within 1σ (same Figure, right panel), with α_γ being slightly shallower than the value of unity predicted by the CR. This shallow slope could be explained by a continuous energy injection (EI), caused, e.g., by prolonged activity of a central engine (Zhang & Mészáros 2001; Zhang et al. 2006). The EI can be characterized by a parameter $q < 1$ such that the continuous luminosity injection is $L(t) \propto t^{-q}$; $q = 1$ means no additional energy injection. The CR for EI in the $\max(\nu_m, \nu_c) < \nu$ regime is $\alpha = (q - 2)/2 + \beta(2 + q)/2$ (Zhang et al. 2006). This yields $q = 0.88 \pm 0.15$ and suggests a mild late-time energy injection.

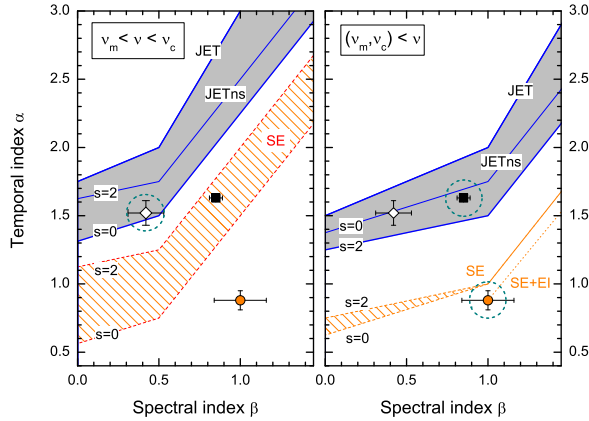


Figure 18. Closure relations (CRs) of the synchrotron forward-shock model. Left and right panels are for the $\nu_m < \nu < \nu_c$ and $\nu_m, \nu_c < \nu$ regimes, respectively. The solid lines and the solid shaded regions indicate CRs for the post-break segment IV of the canonical light curve. The upper and lower boundaries of the solid regions are defined for a jet with (JET) and without (JETns) sideways expansion taken into account, respectively. The dashed lines and hatched regions indicate CRs for the pre-break, spherical geometry (SE). SE accompanied by late-time energy injection (EI) with $q = 0.88$ is shown with the dotted line. Boundary cases for the CBM density profile $n(r) \propto r^{-s}$ are indicated, $s = 0$ (ISM) and $s = 2$ (wind). The small circles stand for the extended γ -ray emission and the squares for the X-ray afterglow. The UVOT temporal index is shown in combination with the spectral index obtained from the broadband SED (open diamonds). The large dashed circles indicate the ejecta geometry and the cooling regime we consider to be likely for the observations (see Section 3.3 for the discussion).

Thus, the CR analysis results in a consistent scenario for the extended γ -ray emission, X-ray, and UV/optical afterglows. The scenario is characterized by a hard electron spectrum, with p in the 1.7–2.0 range, and implies the $\nu_{\text{opt}} < \nu_c < (\nu_X, \nu_\gamma)$ spectral regime for the observations. In this scenario, the X-ray and UV/optical afterglows are observed after the jet break and, assuming a forward-shock origin, the extended γ -ray emission is generated at the pre-break phase of the fireball expansion. These choices are indicated by dashed circles in Figure 18. The temporal slope change $\alpha_X - \alpha_\gamma = 0.75 \pm 0.05$ is in reasonably good agreement ($< 2\sigma$) with the jet break, $\Delta\alpha = 2/3$, expected for the combination of $p \leq 2$, non-spreading jet, and ISM-like environment; when accounting for the late-time energy injection, the agreement is even better. The shallow post-break temporal slope can be explained, in this model, by a “flat” electron spectrum and by a limited lateral spreading of the jet.

We note, that these conclusions are drawn under the assumption of non-transitional regimes for the cooling and the geometry; this approach is justified by the results of our temporal and spectral analysis of the extended emission and the afterglow.

3.4. Extrapolated X-ray Light Curve and Prompt Emission–Afterglow Correlations

Assuming that the power-law energy spectrum measured by Konus-*WIND* at $> T_0 + 30$ s extends unchanged to lower energies, the extrapolated X-ray flux light curve

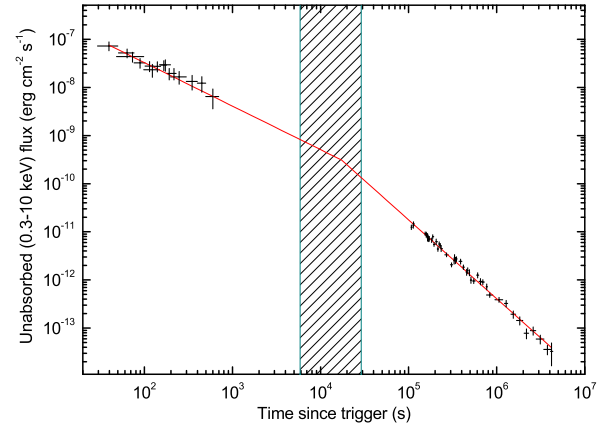


Figure 19. Hypothetical light curve of the GRB 110918A X-ray afterglow constructed from the Konus-*WIND*, SPI-ACS, and XRT observations. Data points prior to $T_0 + 1000$ s are extrapolated from the KW and SPI-ACS data (Section 3.4). The best BPL fit is shown by the solid line and the 1σ break region $(1.74 \pm 1.15) \times 10^4$ s is indicated by the hatched area.

can be calculated from the extended γ -ray emission. The correctness of this approach has been tested, e.g., with the KW data on the “naked-eye” GRB 080319B and the recent nearby GRB 130427A, for which statistically significant tails of an extended emission in the 20–1200 keV band have been observed, both having power-law spectra with $\Gamma \sim 2$. For both GRBs, we found the extrapolated unabsorbed 0.3–10 keV flux to be consistent, within 2–3 σ (or $\leq 20\%$), with simultaneous *Swift*-XRT observations extracted from the XRT light curve repository (Evans et al. 2007, 2009).

Using the KW counts-to-flux conversion factor and the spectral index from the $T_0 + 50 - T_0 + 200$ s interval, we found the extrapolated unabsorbed 0.3–10 keV flux to be in the $(10^{-8} - 10^{-7})$ erg $\text{cm}^{-2} \text{s}^{-1}$ range, which has been previously reported at early phases of bright X-ray afterglows (e.g., GRB 061007, Schady et al. (2007); GRB 080319B, Racusin et al. (2008); GRB 130427A, Evans et al. (2013); Perley et al. (2013)). In Figure 19, a hypothetical light curve, which combines the extrapolated late-time γ -ray observations of GRB 110918A and the XRT afterglow, is shown. Assuming that the accuracy of the extrapolation procedure is comparable to that found for GRB 080319B and GRB 130427A, we added 20% systematics to the statistical-only errors for the extrapolated points. A transition from the initial, flat slope to the final, steeper one occurs in the $T_0 + 10^3 - T_0 + 10^5$ s region, which is not covered by the observations. A simple estimate from the BPL fit to this combined light curve yields, at $\chi_r^2 = 0.97$, the 1σ break region of $t_b = (1.74 \pm 1.15) \times 10^4$ s with pre- and post-break slopes of $\alpha_1 = 0.90 \pm 0.09$ and $\alpha_2 = 1.64 \pm 0.02$, respectively.

In the post-break scenario for the X-ray afterglow, $t_b \sim 1.7 \times 10^4$ s (or ~ 0.2 d) may be considered as a lower limit for t_{jet} , since the extended γ -ray emission cannot be attributed unambiguously to a “plateau” (II) or “normal” (III) phase. In the former case, introducing an additional, “injection” break to the light curve

Table 9
X-ray Afterglow Luminosity

Band (keV)	$L_{X,5}$ (erg s ⁻¹)	$L_{X,1}$ (erg s ⁻¹)	$L_{X,11}$ (erg s ⁻¹)	$L_{X,24}$ (erg s ⁻¹)
0.3–10	1.5×10^{49}	1.7×10^{48}	3.5×10^{46}	1.0×10^{46}
2–10	6.9×10^{48}	7.8×10^{47}	1.8×10^{46}	5.2×10^{45}

Note. — Columns 2 to 4 are the luminosities at 5 minutes, 1 hour, 11 hours, and one day after the trigger in the rest-frame, respectively.

(the break from segment II to segment III) will shift the jet break towards the start of the XRT observations at ~ 107 ks (1.24 d) after the burst. The 0.2–1.24 d range for t_{jet} is consistent with the value suggested from the multi-parameter $E_{\text{iso}} - E_{\text{p},i} - t_{\text{jet}}$ correlation (Liang & Zhang 2005; Ghirlanda et al. 2007), which predicts, for GRB 110918A, the jet break at 0.3 ± 0.13 d using the slopes provided in the latter work.

The isotropic-equivalent K -corrected X-ray luminosity in the rest-frame energy band $E_1 - E_2$ can be calculated from the unabsorbed 0.3–10 keV flux $F_X \propto E^{-\beta_X}$:

$$L_X(t) = 4\pi D_L^2 \frac{F_X[t(1+z)]}{(1+z)^{1-\beta_X}} \frac{(E_2^{1-\beta_X} - E_1^{1-\beta_X})}{(10^{1-\beta_X} - 0.3^{1-\beta_X})}, \quad (6)$$

where E_1 and E_2 are measured in keV. The GRB 110918A afterglow luminosities at 5 minutes, 1 hour, 11 hours, and one day after the trigger in the rest-frame were estimated from the combined extrapolated light curve and are listed in Table 9. We tested the 2–10 keV L_X and the rest-frame prompt emission parameters against $L_X - E_{\text{iso}}$, $L_X - L_{\text{iso}}$, and $L_X - E_{\text{p},i}$ correlations reported by D’Avanzo et al. (2012) from a sample of 56 bright *Swift* GRBs with well-measured X-ray afterglows. GRB 110918A was found to fit these relations within 3σ scatter at all four time marks. The best fit ($\leq 1\sigma$) is for the $L_X - E_{\text{p},i}$ relation; the data are consistently $\sim 2.5 - 3\sigma$ from the $L_X - L_{\text{iso}}$ relation, in general agreement with other correlations for which the extreme L_{iso} of this GRB is considered.

3.5. Jet Opening Angle and Collimation-corrected Energy

In the case of an ISM-like CBM with constant number density n , the jet opening angle is given by Sari et al. (1999):

$$\theta_{\text{jet}} = \frac{1}{6} \left(\frac{t_{\text{jet}}}{1+z} \right)^{3/8} \left(\frac{n\eta_\gamma}{E_{\text{iso},52}} \right)^{1/8}, \quad (7)$$

where η_γ is the radiative efficiency and t_{jet} is measured in days.

For calculations, we adopted canonical values $\eta_\gamma = 0.2$ and $n = 1 \text{ cm}^{-3}$ (Frail et al. 2001). In Table 10, values of θ_{jet} , the collimation factor $(1 - \cos(\theta_{\text{jet}}))$, the collimation-corrected energy release in γ -rays $E_\gamma = E_{\text{iso}}(1 - \cos(\theta_{\text{jet}}))$, and the collimation-corrected peak luminosity $L_\gamma = L_{\text{iso}}(1 - \cos(\theta_{\text{jet}}))$ are listed for the key points of the GRB 110918A observations timeline: $t_{\text{jet}} = 1.2$ d (start of the *Swift* observations), $t_{\text{jet}} = 48$ d (end of the *Swift* observations), and $t_{\text{jet}} = 0.2$ d (a lower limit for the jet break suggested in the previous section).

Table 10
Collimation-corrected energy

t_{jet} (days)	θ_{jet} (deg)	Collimation factor	E_γ (erg)	L_γ (erg s ⁻¹)
0.20	1.7	4.4×10^{-4}	9.2×10^{50}	2.1×10^{51}
1.24	3.4	1.7×10^{-3}	3.6×10^{51}	8.1×10^{51}
>48	>13	$> 2.7 \times 10^{-2}$	$> 5.6 \times 10^{52}$	$> 1.2 \times 10^{53}$

Note. — The estimates are given for an ISM-like CBM with constant number density $n = 1 \text{ cm}^{-3}$; the radiative efficiency $\eta_\gamma = 0.2$ has been assumed.

Figure 20 shows our estimates of the GRB 110918A collimation-corrected energy. For the jet-break time favored from our previous analysis, between 0.2 and 1.24 days (points (a) and (b) in the figure), the implied collimation angle is small, 1.7° – 3.4° , and the inferred values of E_γ and L_γ are in the ranges determined by T13 for the KW GRBs with known collimation factors; also, the E_γ range is effectively the ${}_{-1.5}^{+2.5}\sigma$ scatter of the $E_{\text{p},i} - E_\gamma$ relation (Ghirlanda et al. 2007) calculated at $E_{\text{p},i} = 670$ keV. It should be noted, however, that among such tightly collimated bursts, the fraction of which we estimate to be $< 25\%$ of KW GRBs with known collimation factors, both E_γ and L_γ for GRB 110918A are at the upper edges of their distributions; this implies that the burst’s intrinsic brightness is still remarkable. In the case of a “hidden” break in the afterglow light curve, between points (b) and (c) in Figure 20, the inferred radiated energy still does not move far beyond the observed range $E_\gamma \leq 3.4 \times 10^{52} \text{ erg s}^{-1}$. However, the collimated peak luminosity shifts toward an unprecedented $L_\gamma \sim 10^{53} \text{ erg s}^{-1}$, an order of magnitude higher than the current record.

For a stellar-wind-like environment with $n(r) = 5 \times 10^{11} A_* r^{-2}$, the jet opening angle depends on t_{jet} through (Chevalier & Li 2000):

$$\theta_{\text{jet}} = 0.202 \left(\frac{t_{\text{jet}}}{1+z} \right)^{1/4} \left(\frac{A_* \eta_\gamma}{E_{\text{iso},52}} \right)^{1/4}, \quad (8)$$

where $A_* = (\dot{M}_W / 4\pi V_W) / 5 \times 10^{11} \text{ g cm}^{-1}$ is the wind parameter, \dot{M}_W is the mass-loss rate due to the wind, and V_W is the wind velocity; $A_* \sim 1$ is typical for a Wolf-Rayet star. Although the wind-like CBM is not preferred from our analysis, the θ_{jet} estimate for $A_* = 1$ also results in a tight collimation angle $\sim 4.5^\circ$ and reasonable estimates for $E_\gamma \sim 6.5 \times 10^{51} \text{ erg}$ and $L_\gamma \sim 1.5 \times 10^{52} \text{ erg s}^{-1}$ even at $t_{\text{jet}} = 48$ d.

3.6. GRB 110918A and the Most Luminous GRBs

To date, seven γ -ray bursts with $L_{\text{iso}} > 10^{54} \text{ erg s}^{-1}$ have been observed; Table 11 lists estimates of their rest-frame prompt emission characteristics derived from the Konus-WIND observations. While the scope of this paper does not involve an analysis of this sample, one can see that the GRB 110918A parameters do not differ much from those of other ultraluminous events: almost all of them are hard-spectrum GRBs with a moderately short rest-frame duration.

Notably, none of these bursts (with the exception of GRB 000131, Andersen et al. 2000) demon-

Table 11
The Most Luminous GRBs

Parameter	GRB 110918A ^a	GRB 130505A	GRB 050603	GRB 080916C	GRB 080607	GRB 080721	GRB 000131
z (reference)	0.984 (1)	2.27 (2)	2.821 (3)	4.35 (4)	3.036 (5)	2.591 (6)	4.511 (7)
L_{iso} (10^{54} erg s ⁻¹)	4.7	2.7	2.6	2.4	1.9	1.2	1.1
E_{iso} (10^{54} erg)	2.1 [1.2]	3.8	0.85	4.3	2.0	1.3	1.6
$E_{\text{p,i}}$ (keV)	670 [2000]	2060	1100	2700	1350	1760	700
$T_{90}/(1+z)$ (s)	9.9 [1.3]	6.6	2.9	11.5	7.1	5.4	17.5

References. — (1) Elliott et al. 2013; (2) Tanvir et al. 2013; (3) Berger & Becker 2005; (4) Greiner et al. 2009; (5) Prochaska et al. 2009; (6) Starling et al. 2009; (7) Andersen et al. 2000.

^a Values in square parentheses are for the GRB 110918A initial pulse, the only phase of the burst which could be seen from high redshifts.

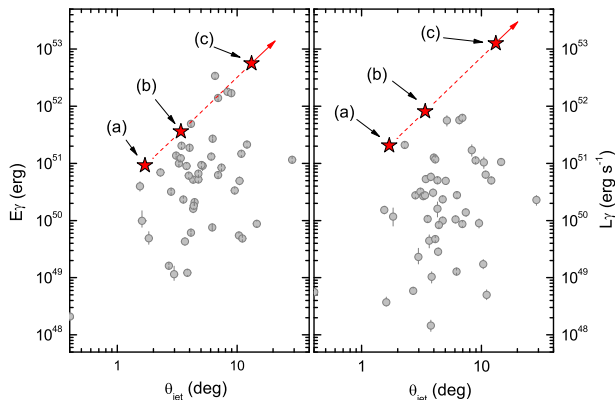


Figure 20. Collimation-corrected energy of the GRB 110918A prompt emission. The collimated energy release E_γ (left) and the collimated peak luminosity L_γ (right) are plotted vs. the collimation angle. Filled stars (a), (b), and (c) show the GRB 110918A energies for an ISM and t_{jet} at 0.2 d, 1.24 d (start of *Swift* observations), and 48 d (end of *Swift* observations), respectively (see Table 10). Gray circles indicate KW GRBs with known collimation factors (Tsvetkova et al., in preparation).

strate a “canonical” steep late-time decay of an afterglow light curve (Grupe et al. 2006; Greiner et al. 2009; Prochaska et al. 2009; Starling et al. 2009). When the late-time temporal and spectral power-law indices of X-ray afterglows are considered, the second and third most luminous GRBs (GRB 130505A¹ and GRB 050603 Grupe et al. 2006) resemble GRB 110918A most closely, suggesting a similar interpretation. Particularly, a flat electron energy spectrum with $p \sim 1.4$ is implied for GRB 050603 by Grupe et al. (2006), as well as a jet scenario for its afterglow observed by *Swift* from 11 hr after the trigger onward. For this burst, the authors estimate a θ_{jet} of 1° – 2° ; a similar collimation angle of $\sim 1.6^\circ$ can be roughly estimated for GRB 130505A from the latest break in its XRT light curve at ~ 29 ks, as suggested by the automated analysis.

4. SUMMARY AND CONCLUSIONS

We have presented the IPN localization and the multi-wavelength study of GRB 110918A, the brightest long

¹ Results of the XRT automated analysis (Evans et al. 2007, 2009) can be found at http://www.swift.ac.uk/xrt_products/00555163

GRB detected by KW during its almost 19 years of observations.

The GRB 110918A prompt emission is characterized by an unprecedented photon flux, whose fast evolution is accompanied by the equally drastic decay of the peak energy of the spectrum. At $z \approx 1$, the huge energy flux measured by *Konus-WIND* implies equally enormous values of the isotropic-equivalent energy in the source frame, making GRB 110918A one of the most energetic and the most luminous γ -ray burst observed since the beginning of the cosmological era in 1997. At the same time we found the key spectral and temporal characteristics of the prompt emission to be in the range typical of other GRBs, suggesting that the same progenitor model for most long bursts is also applicable to GRB 110918A. Having a moderate intrinsic peak energy of the time-integrated spectrum and a typical duration, the burst is close to being a bright outlier of both the Amati and Yonetoku relations; this favors a hypothesis that the huge isotropic-equivalent energy and luminosity result, among other reasons, from a highly collimated emission.

A tail of the soft γ -ray emission was detected out to ~ 700 s after the trigger, with temporal and spectral behavior suggesting an early, bright γ -ray afterglow; these observations partially fill a gap between the prompt emission and the *Swift* observations, which started ~ 1.2 d later. We found the brightness of the early γ -ray and the late-time X-ray afterglows to be in reasonable agreement with reported prompt-afterglow luminosity correlations. This consistency suggests that the mechanism and efficiency of energy transfer from the GRB 110918A central engine to the blast wave and then to the surrounding medium are fundamentally no different from those inherent to most GRBs.

Swift/XRT and *Swift*/UVOT observed the bright afterglow until 48 days after the burst and revealed a steady decline of the X-ray and UV/optical flux with no evidence of a jet break. Our analysis of the multi-wavelength data suggests the post-break scenario for the *Swift*-observed afterglow, with a hard underlying electron spectrum and ISM-like circum-burst environment implied. From the combined light curve, which incorporates the extrapolated early γ -ray afterglow and the late-time XRT observations, we estimate the jet break time to be 0.2–1.2 days. The small implied collimation angle of 1.7° – 3.4° results in reasonable values of the corrected radiated energy and the peak luminosity. We note, however, that, among such tightly collimated events, both E_γ and L_γ for GRB 110918A are on the upper edges of their distributions; this stresses that the burst’s intrinsic

brightness is still outstanding. We conclude, therefore, that the enormous luminosity of GRB 110918A is the result of extreme values for several defining characteristics, in which a highly collimated emission must play a key role.

Finally, we estimate a detection horizon for a similar ultraluminous GRB of $z \sim 7.5$ for Konus-*WIND* and $z \sim 12$ for *Swift*/BAT, which emphasizes the importance of γ -ray bursts as probes of the early Universe.

The Konus-*WIND* experiment is supported by a Russian Space Agency contract, RFBR grants 12-02-00032a and 13-02-12017 ofi-m. KH acknowledges support from NASA grants NNX07AR71G (MESSENGER Participating Scientist Program) and NNX12AE41G (Astrophysics Data Analysis Program). SRO acknowledges support from the UK Space Agency. VM and BS acknowledge financial contribution from the agreement ASI-INAF I/009/10/0.

This work made use of data supplied by the UK Swift Science Data Centre at the University of Leicester.

REFERENCES

- Abdo, A. A., et al. 2009, *Science*, 323, 1688
 Amati, L., Frontera, F., Tavani, M., et al. 2002, *A&A*, 390, 81
 Andersen, M. I., Hjorth, J., Pedersen, H., et al. 2000, *A&A*, 364, L54
 Aptekar, R. L., Frederiks, D. D., Golenetskii, S. V., et al. 1995, *Space Sci. Rev.*, 71, 265
 Arnaud, K. A. 1996, in *ASP Conf. Ser. 101, Astronomical Data Analysis Software and Systems V*, ed. G. Jacoby, & J. Barnes, (San Francisco: ASP), 17
 Band, D., Matteson, J., Ford, L., et al. 1993, *ApJ*, 413, 281
 Band, D. L. 1997, *ApJ*, 486, 928
 Barthelmy, S. D., Barbier, L. M., Cummings, J. R., et al. 2005, *Space Sci. Rev.*, 120, 143
 Berger, E., & Becker, G. 2005, *GCN*, 3520, 1
 Bhat, P. N., Briggs, M. S., Connaughton, V., et al. 2012, *ApJ*, 744, 141
 Breeveld, A. A., Curran, P. A., Hoversten, E. A., et al. 2010, *MNRAS*, 406, 1687
 Breeveld, A. A., Landsman, W., Holland, S. T., et al. 2011, *AIP Conf. Proc.* 1358, 373
 Burrows, D. N., Hill, J. E., Nousek, J. A., et al. 2005, *Space Sci. Rev.*, 120, 165
 Cenko, S. B., et al. 2011, *GCN*, 12367, 1
 Chevalier, R. A., & Li, Z.-Y. 2000, *ApJ*, 536, 195
 D'Avanzo, P., Salvaterra, R., Sbarufatti, B., et al. 2012, *MNRAS*, 425, 506
 Dai, Z. G., & Cheng, K. S. 2001, *ApJ*, 558, L109
 Elliott, J., Kruehler, T., Close, S., et al. 2011, *GCN*, 12366, 1
 Elliott, J., Kruehler, T., Greiner, J., et al. 2013, *A&A*, 556, A23
 Evans, P. A., Beardmore, A. P., Page, K. L., et al. 2007, *A&A*, 469, 379
 Evans, P. A., Beardmore, A. P., Page, K. L., et al. 2009, *MNRAS*, 397, 1177
 Evans, P. A., Page, K. L., Maselli, A., et al. 2013, *GCN*, 14502, 1
 Frail, D. A., Kulkarni, S. R., Sari, R., et al. 2001, *ApJ*, 562, L55
 Frederiks, D., Aptekar, R., Cline, T., et al. 2008, *AIP Conf. Proc.* 1000, 271
 Frederiks, D., & Pal'shin, V. 2011, *GCN*, 12370, 1
 Fruchter, A., Krolik, J. H., & Rhoads, J. E. 2001, *ApJ*, 563, 597
 Ghirlanda, G., Ghisellini, G., & Lazzati, D., 2004, *ApJ*, 616, 331
 Ghirlanda, G., Nava, L., Ghisellini, G., & Firmani, C., 2007, *A&A* 466, 127
 Ghirlanda, G., Nava, L., Ghisellini, G., et al. 2012, *MNRAS*, 420, 483
 Golenetskii, S., et al. 2011, *GCN*, 12362, 1
 Gold, R., Solomon, S., McNutt, R., et al. 2001, *Planet. Space Sci.*, 49, 1467
 Granot, J., & Sari, R. 2002, *ApJ*, 568, 820
 Greiner, J., Clemens, C., Kruehler, T., et al. 2009, *A&A*, 498, 89
 Grupe, D., Brown, P. J., Cummings, J., et al. 2006, *ApJ*, 645, 464
 Guidorzi, C., Kopac, D., & Tanvir, N. R. 2011, *GCN*, 12382, 1
 Hurley, K., Kouveliotou, C., Cline, T., et al. 2000, *ApJ*, 537, 953
 Hurley, K., Mitrofanov, I., Kozyrev, A., et al. 2006, *ApJS*, 164, 124
 Hurley, K., Rowlinson, A., Bellm, E., et al. 2010, *MNRAS*, 403, 342
 Hurley, K., et al. 2011, *GCN*, 12357, 1
 Kalberla, P. M. W., Burton, W. B., Hartmann, D., et al. 2005, *A&A*, 440, 775
 Kobayashi, S., Piran, T., & Sari, R. 1997, *ApJ*, 490, 92
 Kocevski, D., and Liang, E. 2003, *ApJ*, 594, 385
 Kocevski, D., Ryde, F., and Liang, E. 2003, *ApJ*, 596, 389
 Kraft, R. P., Burrows, D. N., & Nousek, J. A. 1991, *ApJ*, 374, 344
 Lee, A., Bloom, E., and Petrosian, V. 2000, *ApJS*, 131, 1
 Lee, A., Bloom, E., and Petrosian, V. 2000, *ApJS*, 131, 21
 Levan, A. J., et al. 2011, *GCN*, 12368, 1
 Lithwick, Y., & Sari, R. 2001, *ApJ*, 555, 540
 Liang, E., & Zhang, B. 2005, *ApJ*, 633, 611
 Liang, E.-W., Racusin, J. L., Zhang, B., Zhang, B.-B., & Burrows, D. N. 2008, *ApJ*, 675, 528
 Liang, E.-W., Yi, S.-X., Zhang, J., et al. 2010, *ApJ*, 725, 2209
 Lü, J., Zou, Y.-C., Lei, W.-H., et al. 2012, *ApJ*, 751, 49
 Mangano, V., et al. 2011, *GCN*, 12364, 1
 Mangano, V., Sbarufatti, B., Evans, P. A., & Krimm, H. A. 2011, *GCN*, 12376, 1
 Mazets, E. P., Cline, T. L., Aptekar, R. L., et al. 1999, *Astronomy Letters*, 25, 635
 Mazets, E. P., Aptekar, R. L., Cline, T. L., et al. 2008, *ApJ*, 680, 545
 Metzger, M. R. et al. 1997, *Nature*, 387, 878
 Norris, J. P., Nemiroff, R. J., Bonnell, J. T., et al. 1996, *ApJ*, 459, 393
 Norris, J. P., Marani, G. F., & Bonnell, J. T. 2000, *ApJ*, 534, 248
 Norris, J. P., Bonnell, J. T., Kazanas, D., et al. 2005, *ApJ*, 627, 324
 Nousek, J. A., Kouveliotou, C., Grupe, D., et al. 2006, *ApJ*, 642, 389
 Nysewander, M., Fruchter, A. S., & Pe'er, A. 2009, *ApJ*, 701, 824
 Oksanen, A., Schaeffer, B., & Templeton, M. 2011, *GCN*, 12369, 1
 Panaitescu, A., & Mészáros, P. 1999, *ApJ*, 526, 707
 Panaitescu, A. 2005, *MNRAS*, 362, 921
 Panaitescu, A., Mészáros, P., Gehrels, N., Burrows, D., & Nousek, J. 2006, *MNRAS*, 366, 1357
 Panaitescu, A. 2007, *MNRAS*, 380, 374
 Pei, Y. S. 1992, *ApJ*, 392, 130
 Perley, D. A., Ganeshalingam, M., Blanchard, P., & Mason, M. 2011, *GCN*, 12388, 1
 Perley, D. A., Morgan, A. N., Urdike, A., et al. 2011, *AJ*, 141, 36
 Perley, D. A., Cenko, S. B., Corsi, A., et al. 2013, *arXiv:1307.4401*
 Poole, T. S., et al. 2008, *MNRAS*, 383, 627
 Prochaska, J. X., Sheffer, Y., Perley, D. A., et al. 2009, *ApJ*, 691, L27
 Racusin, J. L., Karpov, S. V., Sokolowski, M., et al. 2008, *Nature*, 455, 183
 Racusin, J. L., Liang, E. W., Burrows, D. N., Falcone, A., Sakamoto, T., et al. 2009, *ApJ*, 698, 43
 Rau, A., von Kienlin, A., Hurley, K., and Lichti, G., 2005, *A&A* 438, 1175
 Rhoads, J. E. 1999, *ApJ*, 525, 737
 Roming, P. W., Townsley, L. K., Nousek, J. A., et al. 2000, *Proc. SPIE*, 4140, 76
 Roming, P. W. A., Hunsberger, S. D., Mason, K. O., et al. 2004, *Proc. SPIE*, 5165, 262
 Roming, P. W. A., et al. 2005, *Space Science Reviews*, 120, 95
 Ryde, F. 2004, *ApJ*, 614, 827
 Sari, R., Piran, T., & Halpern, J. P. 1999, *ApJ*, 519, L17
 Sari, R., & Piran, T. 1997, *ApJ*, 485, 270
 Sari, R., & Piran, T. 1999, *ApJ*, 520, 641
 Siegel, M. H., Marshall, F. E., De Pasquale, M. & Krimm, H. A. *GCN*, 12371, 1
 Schady, P., de Pasquale, M., Page, M. J., et al. 2007, *MNRAS*, 380, 1041
 Schady, P., Page, M. J., Oates, S. R., et al. 2010, *MNRAS*, 401, 2773
 Schlegel, D. J., Finkbeiner, D. P., & Davis, M. 1998, *ApJ*, 500, 525
 Starling, R. L. C., Rol, E., van der Horst, A. J., et al. 2009, *MNRAS*, 400, 90
 Tanvir, N., Wiersema, K., Levan, A., Greiss, S., & Gaensicke, B., 2011, *GCN*, 12365, 1
 Tanvir, N. R., Levan, A. J., Matulonis, T., & Smith, A. B., 2013, *GCN*, 14567, 1
 de Ugarte Postigo, A., Gorosabel, J., Castro-Tirado, A. J., & Thöne, C. C. 2011, *GCN*, 12375, 1
 de Ugarte Postigo, A., De Breuck, C., Lundgren, A., & Dumke, M. 2011, *GCN*, 12381, 1
 Waxman, E., & Draine, B. T. 2000, *ApJ*, 537, 796
 Yonetoku, D., Murakami, T., Nakamura, T., et al. 2004, *ApJ*, 609, 935
 Zhang, B., Fan, Y. Z., Dyks, J., et al. 2006, *ApJ*, 642, 354
 Zhang, B., & Mészáros, P. 2001, *ApJ*, 552, L35

Zhang, B., & Mészáros, P. 2004, International Journal of Modern
Physics A, 19, 2385
Zou, Y.-C., & Piran, T. 2010, MNRAS, 402, 1854